The Astrophysical Journal Supplement Series, 259:39 (29pp), 2022 April https://doi.org/10.3847/1538-4365/ac480e

Quantum Mechanical Simulations of the Radical–Radical Chemistry on Icy Surfaces

Joan Enrique-Romero[1,2], Albert Rimola[2], Cecilia Ceccarelli[1], Piero Ugliengo[3], Nadia Balucani[1,4,5], and Dimitrios Skouteris[6]

[1] Univ. Grenoble Alpes, CNRS, Institut de Planétologie et d'Astrophysique de Grenoble (IPAG), F-38000 Grenoble, France; juan.enrique-romero@univ-grenoble-alpes.fr
[2] Departament de Química, Universitat Autònoma de Barcelona, Bellaterra, E-08193, Catalonia, Spain
[3] Dipartimento di Chimica and Nanostructured Interfaces and Surfaces (NIS) Centre, Università degli Studi di Torino, via P. Giuria 7, I-10125, Torino, Italy
[4] Dipartimento di Chimica, Biologia e Biotecnologie, Università di Perugia, Via Elce di Sotto 8, I-06123 Perugia, Italy
[5] Osservatorio Astrofisico di Arcetri, Largo E. Fermi 5, I-50125 Firenze, Italy
[6] Master-Tech, I-06123 Perugia, Italy

Received 2021 August 20; revised 2021 December 8; accepted 2021 December 24; published 2022 March 22

Abstract

The formation of the interstellar complex organic molecules (iCOMs) is a hot topic in astrochemistry. One of the main paradigms trying to reproduce the observations postulates that iCOMs are formed on the ice mantles covering the interstellar dust grains as a result of radical–radical coupling reactions. We investigate iCOM formation on the icy surfaces by means of computational quantum mechanical methods. In particular, we study the coupling and direct hydrogen abstraction reactions involving the CH_3 + X systems (X = NH_2, CH_3, HCO, CH_3O, CH_2OH) and HCO + Y (Y = HCO, CH_3O, CH_2OH), plus the CH_2OH + CH_2OH and CH_3O + CH_3O systems. We computed the activation energy barriers of these reactions, as well as the binding energies of all the studied radicals, by means of density functional theory calculations on two ice water models, made of 33 and 18 water molecules. Then, we estimated the efficiency of each reaction using the reaction activation, desorption, and diffusion energies and derived kinetics with the Eyring equations. We find that radical–radical chemistry on surfaces is not as straightforward as usually assumed. In some cases, direct H-abstraction reactions can compete with radical–radical couplings, while in others they may contain large activation energies. Specifically, we found that (i) ethane, methylamine, and ethylene glycol are the only possible products of the relevant radical–radical reactions; (ii) glyoxal, methyl formate, glycolaldehyde, formamide, dimethyl ether, and ethanol formation is likely in competition with the respective H-abstraction products; and (iii) acetaldehyde and dimethyl peroxide do not seem to be likely grain-surface products.

Unified Astronomy Thesaurus concepts: Astrochemistry (75); Reaction rates (2081); Interstellar dust (836); Computational methods (1965); Interstellar molecules (849); Molecule formation (2076)

Supporting material: figure sets

1. Introduction

After the unexpected detection of diatomic molecules in the late 1930s and early 1940s, it was believed that those were the most complex molecules that could be present in the interstellar medium (ISM). The belief was so strong that the searches for more complex interstellar species with radio telescopes were systematically rejected by the telescope allocation committees because they were considered too speculative (Snyder 2006). It was only after 1968/1969, two years that were revolutionary in so many aspects, that polyatomic molecules were detected (Cheung et al. 1968, 1969), and even organic molecules (Snyder et al. 1969).

Among the more than 200 molecular species detected hitherto in the ISM, about one-third contain at least six atoms, among which one or more are carbon atoms. This class of molecules is called interstellar complex organic molecules in the literature (COMs, or iCOMs; Herbst & van Dishoeck 2009; Ceccarelli et al. 2017) and are prevalently, but not exclusively, detected in star-forming regions. They attract a lot of attention for two major reasons. First, they represent the dawn of organic chemistry and could be involved in the emergence of life (e.g., De Duve 2005; de Duve 2011; Ceccarelli et al. 2017). Second, their formation in the harsh ISM environment represents a challenge to astrochemists (e.g., Vasyunin & Herbst 2013; Balucani et al. 2015; Ceccarelli et al. 2017; Jin & Garrod 2020). Since their discovery in the 1970s (Rubin et al. 1971), two competing theories have been proposed to explain the presence and abundances of iCOMs. Either iCOMs are synthesized on the interstellar grain surfaces, or they are synthesized in gas phase by reactions involving simpler grain surface chemistry products. The debate is still vivid, with the weight periodically moving from one to the other.

In both theories, the first step is the formation of icy mantles by hydrogenation reactions of simple species, atoms or molecules, frozen onto the grain surfaces, such as O and CO (Tielens & Hagen 1982). As a result, the dominant species of grain mantles is water, followed by other less abundant species like CO_2, ammonia, methane, and methanol. The subsequent evolution of the icy mantles diverges in the two theories. In the first one, iCOMs are formed in the gas phase during the hot ($\geqslant$100 K) protostellar stage, by reactions involving the components of the sublimated icy mantles (e.g., Charnley et al. 1997; Taquet et al. 2016; Skouteris et al. 2018, 2019; Vazart et al. 2020). In the second theory, it is postulated that, during the cold pre-protostellar stage, the ice components are partially photodissociated by UV photons, generated by the interaction of cosmic rays (CRs) or X-rays with the hydrogen

Table 1
Summary of the Systems and Reactions Studied in This Work

System	Radical Coupling (Rc)	Direct H-abstraction Product 1	Direct H-abstraction Product 2
$CH_3 + CH_3$	C_2H_6 (ethane)		
$CH_3 + NH_2$	CH_3NH_2 (methylamine)		
$CH_3 + CH_3O$	CH_3OCH_3 (dimethyl ether)	$CH_4 + H_2CO$	
$CH_3 + CH_2OH$	CH_3CH_2OH (ethanol)	$CH_4 + H_2CO$	
$HCO + HCO$	HCOCHO (glyoxal)	$CO + H_2CO$	
$HCO + CH_3O$	$HC(O)OCH_3$ (methyl formate)	$CO + CH_3OH$	$H_2CO + H_2CO$
$HCO + CH_2OH$	$HC(O)CH_2OH$ (glycolaldehyde)	$CO + CH_3OH$	$H_2CO + H_2CO$
$CH_3O + CH_3O$	CH_3OOCH_3 (dimethyl peroxide)	$H_2CO + CH_3OH$	
$CH_2OH + CH_2OH$	$CH_2(OH)CH_2OH$ (ethylene glycol)	$H_2CO + CH_3OH$	

atoms in the gas phase, creating radicals that remain trapped in the ices. Once the protostar gradually warms up its surroundings (Viti et al. 2004), these radicals can diffuse over the ice, meet, and react, forming iCOMs (Garrod & Herbst 2006; Garrod et al. 2008; Herbst & van Dishoeck 2009; Kalvāns 2018). Additional processes have been considered to boost the iCOM formation on the icy grain surfaces, such as the reactivity of gas-phase C atoms (Ruaud et al. 2015) or CN (Rimola et al. 2018) landing on the icy surfaces, the formation of glyoxal by the coupling of two HCO radicals formed one next to the other on CO ices, followed by its hydrogenation that leads to glycoaldehyde and ethylene glycol (Simons et al. 2020), or the reactions induced by landing cations on negatively charged icy grains (Rimola et al. 2021).

In this work, we focus on the reactivity on the grain icy surfaces between radicals, arguably the most crucial step of this theory. In astrochemical models, it is usually assumed that when two radicals meet on the grain surfaces, the reaction coupling them into an iCOM is barrierless. Numerically, this is obtained by assuming that the reaction efficiency ε is equal to unity. Here, we present new quantum chemical simulations on nine systems postulated to synthesize iCOMs and observed in the ISM, such as dimethyl ether, methyl formate, and ethanol, in which ϵ is not always equal to 1. Our aim is to compute the activation energy barriers of the reactions forming iCOM and the respective competitive channels employing two ice models representing two different surface environments and the same methodology for all systems. In addition, we compute the approximate efficiency ε of the studied reactions based on the binding and activation barrier energies and provide hints on the possible expected output of other radical–radical systems not studied here and that are of relevance in the formation of iCOMs on the icy surfaces.

The article is organized as follows. In Section 2, we present the systems studied in this work and the previous studies on which the present one is based. In Sections 3 and 4, we describe the adopted methodology and the results of the new computations, respectively. In Section 5, we discuss the results, and Section 6 concludes the article.

2. Previous Works and Present Studied Systems

Several theoretical studies on the chemistry of the interstellar icy surfaces have appeared in the literature during the past decade. A recent general review can be found in Zamirri et al. (2019). Here we focus on the studies involving radical–radical reactions on the icy surfaces. Other studies have considered pure CO ices (Lamberts et al. 2019), where the bonds between the species and the surface are substantially different and much less strong with respect to water ices.

The new study presented in this work is based on previous ones from our groups, described here. We presented a first pioneer study of the two systems $HCO + CH_3$ and $HCO + NH_2$ in previous works (Rimola et al. 2018; Enrique-Romero et al. 2019), as well as an in-depth study on the accuracy of the adopted methodology (Enrique-Romero et al. 2020). In the present work, we expand the number of systems studied in Enrique-Romero et al. (2019), adding nine more cases. Specifically, we selected a subset of the radical species considered by Garrod et al. (2008) and that are the photolysis products of the closed-shell species formaldehyde, methane, methanol, and ammonia: CH_3, HCO, CH_3O, CH_2OH, and NH_2. Among those radicals, here we focus on the $CH_3 + X$ and HCO + Y systems, where $X = NH_2$, CH_3, HCO, CH_3O, CH_2OH and $Y = HCO$, CH_3O, CH_2OH. The list of studied systems and the possible products (from radical combination and direct H abstraction, respectively) are summarized in Table 1.

Our first goal here is to provide the potential energy surface (PES) of the reactions of the above systems, namely, the energetics of the radical–radical coupling (hereinafter Rc) reaction, leading to the formation of an iCOM, as well as the possible competitive channels. In this respect, the previous studies mentioned above have shown that the H-abstraction reactions can potentially be more energetically favorable than the simple combination of the two radicals. In general, for H-abstraction reactions to take place, H-donor and H-acceptor radicals are needed. In some cases, such as $CH_3 + CH_3$, it does not happen. In others cases, such as $HCO + CH_3O$, both radicals can act as either H acceptors or H donors so that two direct H-abstraction channels might exist with different products.

In Enrique-Romero et al. (2019), we carried out the calculations considering two models for the amorphous water surfaces, with 18 (W18) and 33 (W33) waters. The W33 model is large enough to possess a geometrical cavity where radicals can lie, whereas the W18 model is too small for that purpose and only a "flat" surface is possible. These two models are obviously rough analogs of the ices that cover the interstellar

grains. Nonetheless, they allow estimates of the energetics of reactions of radicals sitting on flat surfaces and inside a cavity, respectively. The latter is particularly interesting to describe the likely situation of most frozen radicals, as they are believed to be formed by the UV irradiation of the ice bulk. In other words, reactions among radicals are much more likely to occur in situ ations where they are surrounded by water molecules than on a flat surface exposed to the gas phase. Actually, it is even possible that our W33 cavity description provides an optimistic view, as radicals may even be trapped in frozen water cages. For these reasons, in this work we will pay special attention to the reactions occurring in the W33 cavity.

Providing the energetic of the process is a first mandatory step, but it is not the end of the story. Following the study by Enrique-Romero et al. (2021), further kinetics calculations will then provide estimates of the efficiency of the formation of the iCOMs on the icy grain surfaces via the radical–radical coupling and the H-abstraction competitive products, respectively. This study on the kinetics is postponed to a forthcoming article.

It is worth mentioning that the present work holds some limitations. Radical–radical chemical reactions on top of these two cluster surface models were explored by considering a single reaction site on each model for reaction. This is motivated by the large number of investigated reactions (see Table 1) and the relatively high computational cost of the simulations we have carried out, especially when dealing with reactivity. However, by means of this approach, we represent two different surface morphological situations, namely, reactions taking place on a rather flat surface and on a small cavity (W18 and W33, respectively). Similarly, for the computations on the binding energies (see also Section 3.3) of each radical interacting with the surfaces, a single binding site for each radical on top of each ice model was investigated. This is indeed a simplistic assumption given that different surface binding sites are available and, accordingly, a distribution of binding energies exist (e.g., Bovolenta et al. 2020; Ferrero et al. 2020; Duflot et al. 2021). Finally, diffusion has not explicitly been studied in this work given the rather small size of our ice models. In order to properly study surface diffusion, one would need a much larger ice model with well-characterized diffusion barriers (see, e.g., Senevirathne et al. 2017). In those cases where diffusion energies were needed, they were just approximated as a fraction of the calculated binding energies (see Section 3.4), as usually done in astrochemical modeling.

3. Methods

In this section, we present the adopted amorphous solid water (ASW) ice models, the methods employed for the electronic structure calculations, and, finally, how binding energies were calculated.

3.1. Water-ice Models

Following Enrique-Romero et al. (2019), two cluster models have been used to simulate the surfaces of interstellar ASW (shown in Figure 1). They consist of 18 and 33 water molecules, which will be hereafter referred to as W18 and W33, respectively. The dimensions of the ice models slightly changed with respect to those reported in Enrique-Romero et al. (2019) owing to using an improved dispersion correction term in the geometry optimizations (namely, the D3(BJ) dispersion instead of the bare D3 one). Interestingly, as highlighted in Figure 1, while W18 presents a flat surface morphology (of $\sim$11.2 $\times$ 6.7 Å), this is not the case for W33, which presents two different regions: a 6 Å wide cavity, and its elongated side (13.8 Å long). However, in this work, at variance with Enrique-Romero et al. (2019), for W33 calculations, only the cavity structure has been considered. The reason for this choice relies on the fact that, as shown in Enrique-Romero et al. (2019), results provided by W18 and by W33's elongated side are very similar. Additionally, we have also found that, for some radical–radical reactions, dramatic structural changes occurred on the W33 cluster model, in which the cavity collapsed when reactions between highly bound species were simulated. Both ice surfaces have a thickness of about 6–7 Å.

3.2. Electronic Structure Calculations

All density functional theory (DFT) calculations were run with the GAUSSIAN16 software package (Frisch et al. 2016). Following our previous work, the BHLYP functional (Lee et al. 1988; Becke 1993) was used, in which Grimme's three-body dispersion correction, alongside the Becke-Johnson damping function (D3(BJ); Grimme et al. 2010, 2011), was introduced in a posteriori manner.

The radical–radical reactions were studied both on ASW surface models and in the absence of water molecules.[7] For the former, demanding calculations like geometry optimizations or frequency calculations were run by using the double-ζ Pople's basis set 6-31+G(d,p) (Hehre et al. 1972; Hariharan & Pople 1973), which were later refined by single-point calculations with the 6-311++G(2df,2pd) (Krishnan et al. 1980) basis set. For the latter, due to their less demanding computational effort, all geometry optimizations were performed with the 6-311++G(2df,2pd) basis set.

All stationary points were characterized by the analytical calculation of the harmonic frequencies as minima (reactants, products, and intermediates) and saddle points (transition states). Intrinsic reaction coordinate (IRC) calculations at the same level of theory were carried out (when needed) to ensure that the transition states connect with the corresponding minima. Thermochemical corrections to the potential energy values were carried out using the standard rigid rotor/harmonic oscillator formulae to compute the zero-point energy (ZPE) corrections (McQuarrie 1976). In order to properly simulate singlet electronic state biradical systems, we used the unrestricted formalism alongside the broken (spin) symmetry (BS) approach (e.g., Neese 2004), which has been proven to be a cost-effective methodology to properly describe the electronic structure of these kinds of systems, reaching good agreement with highly correlated methods (Enrique-Romero et al. 2020, 2021). In the BS approach, singlet and triple states are mixed. This allows each unpaired electron to be localized on top of each radical (see Table 10 in Appendix G and the supporting figures available on Zenodo at doi:10.5281/zenodo.5723996), at the expense of having a nonuniform spin density with positive spin density on one of the radicals and negative spin density on the other. The BS singlet state is not a solution of the $\hat{S}^2$ operator, and therefore $\langle S^2 \rangle$ is not equal to 0 but is 1 for a singlet biradical system, i.e., a mixture between

[7] That is, the reaction between the two radicals alone, in order to assess whether radicals are able to directly react or not.

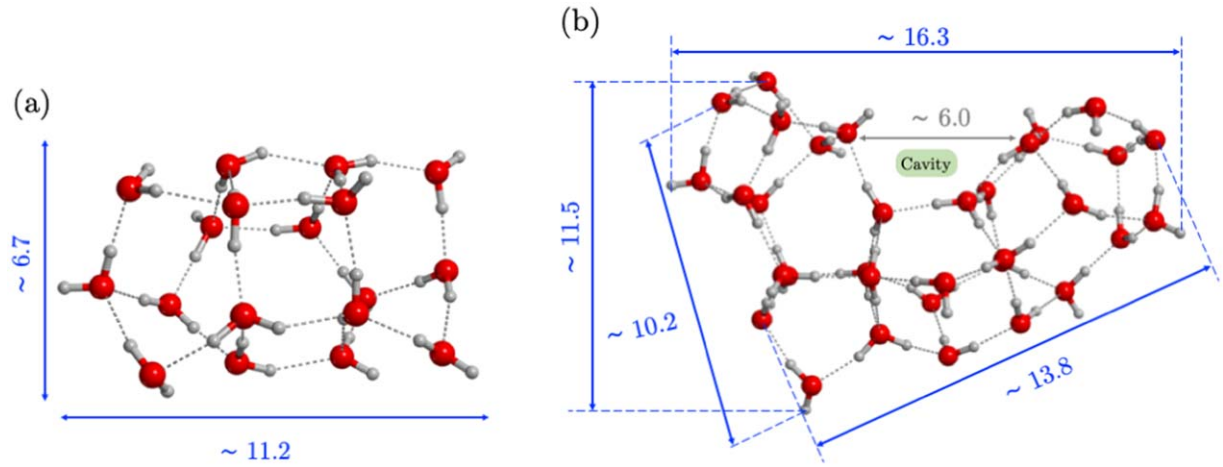

Figure 1. ASW models used in this work. The geometries were optimized at BHLYP-D3(BJ)/6-31+G(d,p) level. Distances in angstroms.

singlet and triplet states. Spin contamination issues may appear; however, we do not observe it in any of our systems as indicated by the spin annihilation step automatically run by GAUSSIAN16, with errors lower than 10% with respect to the pure singlet, as can be seen in Tables 11 and 12 in Appendix H.

Finally, we also calculated the tunneling crossover temperatures (T_c) following Fermann & Auerbach (2000; see Appendix J for more details) for those reaction steps where a hydrogen atom is transferred.

3.3. Binding Energies

The calculations of the radical–surface binding energies adopted the same electronic structure methodology as for reactivity. That is, for each radical–surface complex and isolated components (i.e., radicals and surfaces), geometry optimizations and frequency calculations (and hence ZPE corrections) were computed at the BHLYP-D3(BJ)/6-31+G(d,p) level, which were followed by single-point energy calculations at the improved BHLYP-D3(BJ)/6-311++G(2df,2pd) level to refine the potential energy values. With the obtained values we calculated the dispersion and deformation-corrected interaction energies ($\Delta E_{\rm ads}$).

Subsequently, basis set superposition error (BSSE) corrections were obtained by running single-point energy calculations at the BHLYP-D3(BJ)/6-311++G(2df,2pd) theory level. This means that BSSE was corrected in a posteriori fashion to the optimization of the complexes, i.e., it was not accounted for during the geometry relaxation. The final, corrected interaction energy ($\Delta E^{\rm CP}_{\rm ads}$) was calculated using the following equation:

$$\Delta E^{\rm CP}_{\rm ads}(AB) = \Delta E_{\rm ads} + {\rm BSSE}(A) + {\rm BSSE}(B) + \Delta {\rm ZPE}. \quad (1)$$

Note that we used the same sign convention as in Enrique-Romero et al. (2019), namely, $\Delta E^{\rm CP}_{\rm ads} = -\Delta E^{\rm CP}_{\rm bind}$, and that $\Delta E_{\rm ads}$ already contain the contributions of the deformation owing to the formation of the surface–radical complex.

3.4. Reaction Efficiencies

Astrochemical models compute the abundance of species by solving time-dependent equations that equate formation and destruction rates for each species. For grain-surface reactions, the formation rate is determined by the rate of encounters of the two reactants on the reaction site multiplied by the efficiency of the reaction, ε, which is the probability that when the two reactants meet they also react (Hasegawa & Herbst 1993; Garrod & Herbst 2006).

In order to provide a rough estimate of ε, we used the activation energy barriers and binding energies, following the schemes commonly used in astrochemical models (see Enrique-Romero et al. 2021, for a detailed discussion):

$$\varepsilon = \frac{k_{\rm aeb}}{k_{\rm aeb} + k_{\rm diff,1} + k_{\rm des,1} + k_{\rm diff,2} + k_{\rm des,2}}, \quad (2)$$

where $k_{\rm aeb}$ are the rate constants related to the activation energy barrier and $k_{{\rm diff},i}$, $k_{{\rm des},i}$ are the diffusion and desorption rate constants of the species i.

All of these rate constants were derived using the Eyring equation:

$$k = (k_{\rm B}T/h)\exp(-E_a/k_{\rm B}T), \quad (3)$$

where $k_{\rm B}$ and h are the Boltzmann and Planck constants, T is the (surface) temperature, and E_a is the activation energy of the process, i.e., the activation energy barrier for reactions or the diffusion $E_{\rm diff}$ and desorption $E_{\rm des}$ energies. It is worth noting that in Equation (2), entropic effects are neglected, which is consistent with the very low temperature at which the processes (chemical reaction, diffusion, desorption) take place. The desorption energy, responsible for the $k_{{\rm des},1/2}$ terms, is just the opposite of the binding energy of each species, while the diffusion energy is taken to be a fraction of the desorption one.

In the literature, the $E_{\rm diff}/E_{\rm des}$ ratio is usually assumed to be in the range of 0.3 and 0.4 for molecules (e.g., Hasegawa et al. 1992; Karssemeijer & Cuppen 2014; Ruaud et al. 2016; Penteado et al. 2017; Aikawa et al. 2020; Jin & Garrod 2020). Recently, He et al. (2018) were able to measure the diffusion barrier of a number of molecules on ASW ices. They found $E_{\rm diff}/E_{\rm des}$ ratios ranging between ~0.3 and 0.6, depending on the coverage of admolecules, so that little coverage (sub-monolayer, ML, of admolecules) corresponds to the lower end of the $E_{\rm diff}/E_{\rm des}$ ratio range, while higher coverages (>1 ML) correspond to the higher end of the ratio range. Larger values of $E_{\rm diff}/E_{\rm des}$ are normally assumed for atomic species (e.g., Minissale et al. 2016 found experimentally an $E_{\rm diff}/E_{\rm des}$ value of 0.55 for N and O), and in the literature there is a fairly large amount of work in which a value of 0.5 is assumed (e.g., Garrod & Herbst 2006; Garrod et al. 2008; Garrod & Pauly 2011; Ruaud et al. 2015; Vasyunin et al. 2017; Jensen

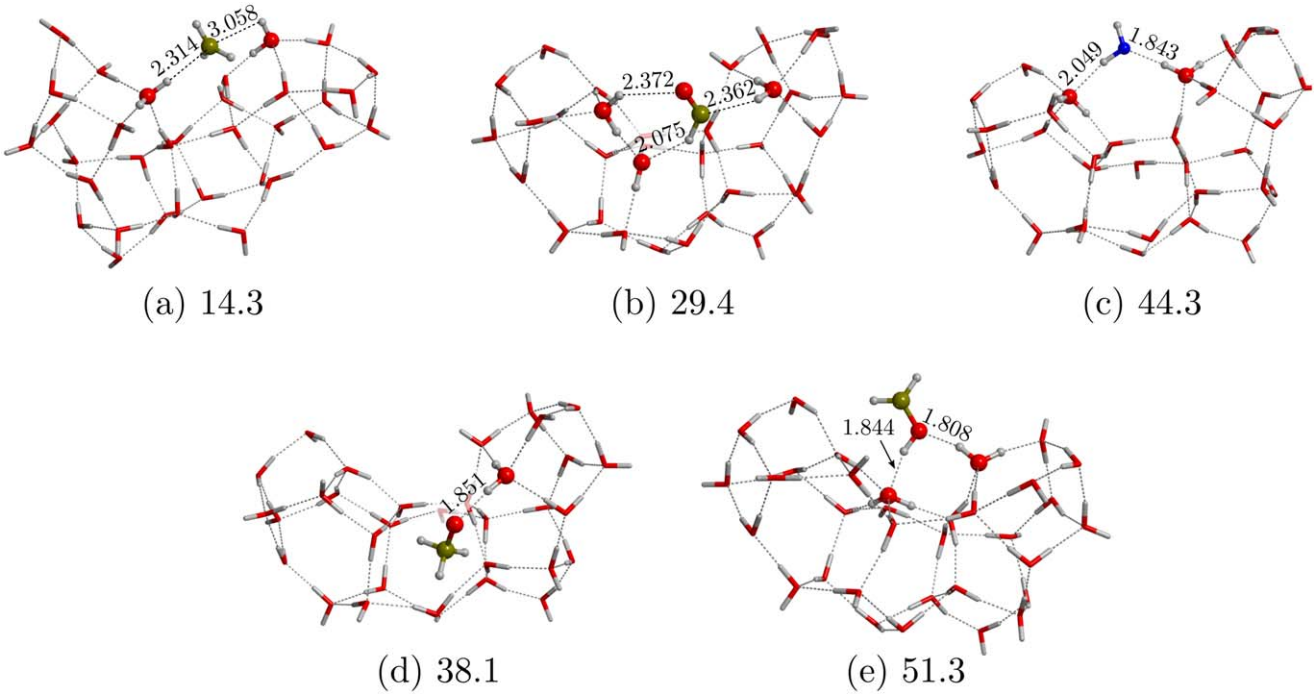

Figure 2. Geometries of the five studied radicals, (a) CH_3, (b) HCO, (c) NH_2, (d) CH_3O, and (e) CH_2H, adsorbed on W33 fully optimized at the UBHLYP-D3(BJ)/6-31+G(d,p) theory level. Energy values in kJ mol^{-1} are those refined at the BHLYP-D3(BJ)/6-311++G(2df,2pd) level with the ZPE and BSSE corrections. Distances in angstroms.

Table 2
Computed Corrected Binding Energies (ΔE_{bind}^{CP}) for the Radicals Interacting with the W18 and W33 Cluster Models

ΔE_{bind}^{CP}	CH_3	HCO	NH_2	CH_3O	CH_2OH
W33	14.3	29.4	44.3	38.1	51.3
W18	8.1	20.5	31.8	26.1	45.9

Note. Units are in kJ mol^{-1}. The components of each binding energy are available in Appendix D, in Table 6.

et al. 2021). This can, however, cause surface reactions to be much more efficient than using the recommended 0.3–0.4 range, as shown and discussed in detail by Enrique-Romero et al. (2021). For this reason, we used an intermediate value for E_{diff}/E_{des} of 0.35 in order to calculate the efficiency of the radical–radical reactions presented in this work.

4. Results

4.1. Binding Energies

The computed binding energies of the studied radicals with W33 and W18 are reported in Table 2. Optimized geometries for W33 are reported in Figure 2, while those for W18 are available in Figure B1 in Appendix B. For CH_3, HCO, and NH_2, complexes in Enrique-Romero et al. (2019) were reoptimized at the current theory level. For CH_3O and CH_2OH, the initial structures were constructed by maximizing the intermolecular interactions between the radicals and the cluster models.

Computed binding energies follow the order of $CH_3 < HCO < NH_2 < CH_3O < CH_2OH$.

Differences with respect to binding-energy values in Enrique-Romero et al. (2019) arise from the different dispersion terms used in the two works, namely, D3(BJ) here versus D3 in Enrique-Romero et al. (2019), in which the former is understood to be more accurate as the components defining the D3(BJ) term enter in an optimization process in agreement with the particular system to simulate. Nevertheless, the same binding-energy trends are obtained for the CH_3, HCO, and NH_2 cases.

Interestingly, binding energies on W33 are about 12%–76% higher than on W18, showing the importance of the larger number of intermolecular interactions formed in the former cluster, as well as the larger dispersion interactions that originate when the radicals adsorb in the cavity.

The reliability of our methodology in computing these binding-energy values is evidenced by comparing the results at BHLYP-D3(BJ)/6-311++G(2df,2pd) with those at the CCSD(T)/aug-cc-pVTZ level (single-point energy calculations on the BHLYP-D3(BJ) optimized geometries), in which a very good correlation between values is obtained (see Figure A2 in Appendix A).

4.2. Radical–Radical Reactivity

In this section, the reactivity of the different sets of radical pairs on the W33 and W18 surface cluster models is presented. For the sake of clarity and brevity, along this section only structures involving W33 are shown. However, all computed structures, i.e., all the stationary points for both W33 and W18, are available in Figures 3 and 5.

Remarkably, we showed in previous publications (Enrique-Romero et al. 2019, 2020) that water-assisted hydrogen transfer reactions present multiple steps and exceedingly high activation energies to be surmountable at interstellar conditions, so that these paths have been excluded in this work. Therefore, here we focus on the radical–radical coupling (Rc) leading to the formation of iCOMs (e.g., $CH_3 + CH_3O \rightarrow CH_3OCH_3$) and

the direct hydrogen abstraction (hereinafter dHa) leading to simpler products (e.g., $CH_3 + CH_3O \rightarrow CH_4 + H_2CO$).

It is worth reminding that dHa reactions are not possible in the cases of $CH_3 + CH_3$ and $CH_3 + NH_2$, since none of these radicals can behave as H donors (i.e., these reactions would be endothermic). In contrast, for radical pairs in which both reactants exhibit properties of H acceptors and H donors, such as HCO, CH_3O, and CH_2OH, two possible dHa processes are investigated (from each species, respectively). However, here we only show the most energetically favorable Rc and dHa channels. The energetic data of all the computed reactions on both ice models are available in Tables 7–9 in Appendix E.

In the following, we will discuss the results separating the reactions into three groups, for better clarity: (i) reactions of $CH_3 + X$, (ii) reactions of HCO + X, and (iii) reactions of $CH_3O + CH_3O$ and $CH_2OH + CH_2OH$.

4.2.1. $CH_3 + X$ Reactions

In general, these kinds of reactions have very low energy barriers unless CH_3 is trapped by surrounding water molecules in the ice structure incrementing the energy barriers due to steric effects, as is the case of $CH_3 + CH_3O$ (both Rc and dHa channels) and $CH_3 + CH_3$ (see Figure 3). Another source of high-energy barriers is when the radical partner experiences a strong attachment with the surface, which has to be broken for the reaction to take place. This is the case of the $CH_3 + CH_2OH$ dHa reaction.

$CH_3 + CH_3$. This reaction, which can only lead to ethane formation through the Rc channel, is barrierless on W18. In contrast, on W33, despite that the CH_3/surface interactions are essentially via dispersive forces (Enrique-Romero et al. 2019), the reaction has a net energy barrier of 4.6 kJ mol^{-1}. The origin of this energy barrier arises from the interaction of one CH_3 with the water molecules of the surfaces. Indeed, in the reactant structure, one CH_3 is trapped by two dangling water surface H atoms, this way establishing weak H-bond interactions and reinforcing the dispersion interaction contribution. This "blocked" CH_3 radical needs to move against the surrounding water molecules, which requires a certain amount of energy. This can be seen by the change in the bare interaction energies (i.e., non-corrected for ZPE and BSSE) of the blocked CH_3 radical with the surface in reactants (24.6 kJ mol^{-1}) and in the TS (15.6 kJ mol^{-1}), where the TS has a much less stable CH_3 adsorption situation (by 9.1 kJ mol^{-1}).

Interestingly, these two weakly C–H $\cdots$ O interactions are only possible on W33 owing to the surface morphology of the cluster. Conversely, on W18, this interaction is not present (the two C–H $\cdots$ O dangling bonds are missing) and, accordingly, the Rc reaction proceeds in a barrierless fashion.

$CH_3 + NH_2$. As in the previous case, reaction between CH_3 and NH_2 only leads to the formation of the iCOM (Rc channel), in this case methylamine (CH_3NH_2). For this radical pair, product formation presents very low energy barriers (0.4/1.6 kJ mol^{-1} on W33/W18). This is because the transition states mainly involve a translation/rotation of CH_3 toward NH_2.

$CH_3 + CH_3O$. The formation of dimethyl ether (CH_3OCH_3) through the Rc channel on W18 has a barrier 0.2 kJ mol^{-1}, while on W33 it has a barrier of 3.1 kJ mol^{-1}. This reaction is barrierless when we do not consider any ASW model (as in practice on W18); therefore, the origin of the barrier on W33 is caused by the morphology of the cluster model, similarly to what happens to the $CH_3 + CH_3$ case. Indeed, also in this case, the CH_3 establishes weak H-bond interactions, which have to be broken to couple with the O of CH_3O. The difference in the interaction energies of the CH_3 radical with the surface between reactants (interaction energy of 24.4 kJ mol^{-1}) and the transition state (interaction energy of 17.1 kJ mol^{-1}) is 7.3 kJ mol^{-1} (not corrected for ZPE and BSSE), while for the CH_3O radical it is rather small, just 0.4 kJ mol^{-1}. The dHa channel leading to $CH_4 + H_2CO$ presents activation barriers of 9.5 and 1.0 kJ mol^{-1} on W33 and W18, respectively. In the absence of water molecules this reaction has a barrier of 1.7 kJ mol^{-1} associated with the H–CH_2O bond breaking. This indicates that the energy barrier on W18 arises from this weak H-bond breaking, while on W33 it also has contributions from cavity effects. In the latter case, the high barrier is due to the combined effect of (i) the blocking of the CH_3 radical and (ii) the steric effects arising from the dispersion forces between the –CH_3 moiety of CH_3O and the surface in order to reach a proper orientation allowing the H transfer. Overall, the CH_3 radical experiences a change in interaction energies with the surface of 13.5 kJ mol^{-1}; CH_3O, of 6.0 kJ mol^{-1}.

$CH_3 + CH_2OH$. This radical pair presents very low energy barriers in the Rc channel to form ethanol (CH_3CH_2OH), of 2.5 and 1.9 kJ mol^{-1} on W33 and W18, respectively. The opposite occurs for the dHa channel to form $CH_4 + H_2CO$ (39.0 and 32.2 kJ mol^{-1} on W33 and W18, respectively). Although the interaction of CH_2OH with the surface is strong owing to stable H bonds, these H bonds do not affect the Rc channel, since the unpaired electron is on the C atom, which is freely accessible for the coupling. Accordingly, the Rc channel only requires overcoming the CH_3/surface dispersion interactions to form the C–C bond. In contrast, for the dHa channel, the strong CH_2OH/surface H-bond interactions inhibit the reaction since the H to be transferred is participating in the H bonds, requiring the breaking of these interactions. The cost of this action is reflected by the fact that, in the absence of water molecules, the dHa channel has a lower energy barrier, of 9.8 kJ mol^{-1}.

4.2.2. HCO + X

In contrast to the previous set of reactions, HCO + X (see Figure 4) have slightly higher energy barriers owing to the higher binding energy of HCO. Nevertheless, HCO is a relatively good H donor, and therefore dHa reactions in which HCO donates its H atom have similar energy barriers to those of Rc.

HCO + HCO. The energy barriers for Rc forming glyoxal (HCOCHO) and for dHa forming CO + H_2CO are very similar, i.e., 4.1 and 4.0 kJ mol^{-1} for Rc and 4.0 and 2.7 kJ mol^{-1} for dHa on the W33 and W18 surfaces, respectively. Here, the energy barriers are very similar because in both paths the structural reorganization of the reactants leading to products is also similar. Indeed, the reactions mainly involve the rotation of one of the two HCO radicals to arrive at the proper orientation to form either HCOCHO or CO + H_2CO, with a similar energy cost.

HCO + CH_3O. For this system, the Rc and dHa channels (forming methyl formate and CO + CH_3OH, respectively) on W33 and W18 present similar energy barriers, of 3.5 and 5.1 kJ mol^{-1} and 2.0 and 3.2 kJ mol^{-1}, respectively. This is because the reactions proceed either through the translation (Rc) or the rotation (dHa) of the HCO radical, which present a similar energy cost. It is worth mentioning that this biradical system can also present another dHa channel, in which the CH_3O

transfers its H atom to HCO to form $H_2CO + H_2CO$. However, this channel has a higher energy barrier (13.3/9.6 kJ mol^{-1} on W33/W18) because the orientation of CH_3O to transfer its H requires the breaking of the CH_3O/surface interactions. This was also observed in other radical pairs in which CH_3O is the H donor in dHa processes (e.g., $CH_3 + CH_3O$).

$HCO + CH_2OH$. The reactivity of this biradical system is similar to the previous one. That is, both the Rc channel (forming glycolaldehyde) and the dHa channel (in this case forming $CO + CH_3OH$ owing to the H transfer from HCO to CH_2OH) present energy barriers below ∼2 kJ mol^{-1}, irrespective of the surface model where they are calculated. The explanation is the same: since CH_2OH is firmly attached by H bonds on the surface, the reactions are driven by the motion of HCO, which in practice does not present any energy cost. Similarly to the previous biradical system, another dHa channel has been identified: that in which the H transfer takes place from CH_2OH to HCO forming $H_2CO + H_2CO$. Also in this case, the energy barriers are as high as ∼18 kJ mol^{-1} (on W33; see Figure 3) owing to the energy cost to break the CH_2OH/surface interactions, which is mandatory to transfer the H atom. The same reaction in the absence of water presents a barrier of 8.8 kJ mol^{-1}, indicating that this structural reorganization is hindered by the CH_2OH/surface H bonds.

4.2.3. $CH_3O + CH_3O$ and $CH_2OH + CH_2OH$

As was seen above, the reactivities of $CH_2OH + X$ and CH_3O+X (where X = CH_3 and HCO, see Figure 5) share some similar aspects, namely, Rc and dHa (where neither CH_3O nor CH_2OH acts as an H donor) reactions tend to have low energy barriers. However, high energy barriers appear when either CH_3O or CH_2OH acts as an H donor in dHa reactions.

In the $CH_3O + CH_3O$ and $CH_2OH + CH_2OH$ cases, we observed a clearly different reactivity for their coupling reactions. In the $CH_3O + CH_3O$ system, the Rc channel presents high energy barriers, given that the unpaired electrons on the O atoms are less reactive as a consequence of the H-bonding interaction with the surface, while for the $CH_2OH + CH_2OH$ case, very low activation energies are obtained for the Rc channel on either surface model as a consequence of CH_2OH binding mode. Regarding their dHa reactions, we observe high energy barriers for both systems, as observed for $CH_2OH + CH_3$/HCO and $CH_3O + CH_3$/HCO, where CH_2OH/CH_3O acts as the H donor.

$CH_3O + CH_3O$. The Rc channel between two CH_3O radicals on W33 has a higher energy barrier than the dHa one (20.1 and 11.7 kJ mol^{-1}, respectively). This is because, in the reactant structure, both CH_3O radicals establish H-bond interactions with the surface through their O atoms. Since the Rc channel involves the coupling of the unpaired electrons of the two O atoms, the reaction requires the breaking of these H bonds in both species. The contribution of these H-bond interactions in this energy barrier is demonstrated by the calculated value of the barrier in absence of water, of 1.8 kJ mol^{-1}. In the dHa channel, in contrast, an H atom is transferred from one CH_3O to the other without the need to break these H bonds. In this case, the reorientation of the radicals is enough to facilitate the H transfer.

However, on W18 we observe the opposite trend: the Rc channel presents a lower energy barrier than the dHa one (10.3 and 15.9 kJ mol^{-1}, respectively). This is because in the reactant structure there are fewer intermolecular interactions and the two radicals are well oriented for the coupling, something that cannot take place in the cavity model owing to its size and the lack of well-oriented binding sites.

$CH_2OH + CH_2OH$. This system is a paradigmatic case in which the Rc channel has a low energy barrier while the dHa ones do not. Indeed, the lowest energy path is the Rc one, with 2.6/4.4 kJ mol^{-1} on W33/W18. On both clusters, the reaction involves a simple rotation around the intermolecular C–C dihedral angle (e.g., see the Rc path in Figure 5(b)) in such a way that once the C atoms of each radical face one another the system easily evolves to form $CH_2(OH)CH_2OH$ (ethylene glycol) as a product.

In contrast, dHa reactions present higher energy barriers, about 9.1/20.6 kJ mol^{-1} on W33/W18, and often have multiple reorientation steps before the actual H abstraction takes place; see, for example, the dHa1 and dHa2 channels on W33 shown in Figure Set 3 and Figure 5(b), respectively. These are the consequences of the intrinsic stability of the CH_2OH radical (in the absence of water molecules, two CH_2OH radicals are able to form stable dimers) and the high capacity of this radical.

4.2.4. Summary of Radical–Radical Reactivity

The results on the activation barriers for each studied system and reaction are listed in Table 3. In this table, we report the highest energy barriers (including ZPE corrections), if any, of the least energetic path for Rc and dHa reactions, respectively, for both W33 and W18 ice models and in the absence of any ASW model. For those cases in which the PES has more than one reaction step (for example, the dHa-CH_2OH/$CH_2OH \cdots$ W33; Figure 5), only the highest barrier of the sequence is reported. Likewise, for those cases where two dHa channels exist, only the highest barrier of the most favorable channel (according to the activation energies) is reported.

Table 3 also reports the reaction energy for all the studied reactions.

4.3. Reaction Efficiencies

As described in Section 3, we computed a rough estimate of the efficiency of the reactions, ε, following Equation (2), using the computed binding energies of the radicals (Table 2, assuming an $E_{\rm diff}/E_{\rm des}$ ratio of 0.35) and the activation energy barriers of the reactions (Table 3). Quantum tunneling effects are included in a qualitative manner on dHa reactions via their crossover temperatures (T_c; see Appendix J).

With these calculations we aim to provide a simple means to discriminate which radical–radical processes are likely efficient from those that are not. In order to do this, we provide the efficiency values at the highest temperature possible for each reaction. In the absence of a full astrochemical model, we calculate this upper-limit temperature as the temperature at which one would expect radicals to disappear from the surface owing to thermal desorption. This is achieved by matching the desorption timescale (proportional to $1/k_{\rm des}$) to a value of 1 Myr (corresponding to the typical age expected for a protostar), which provides us with a temperature value. We label these temperatures by $T_{\rm des}$, and they are listed in Tables 4 and 5 for the W33 and W18 ice models, respectively, together with the efficiencies for the radical coupling and direct H-abstraction reactions at these temperatures, and at 10 K.

Table 3
Summary of the Theoretical Results for Radical–Radical Reactivity

System	Ice Model	Radical–radical Coupling			Direct H Abstraction				Reaction Category
		Product	$\Delta H^{\ddagger}$	ΔH^{reac}	Product	$\Delta H^{\ddagger}$	ΔH^{reac}	T_c (K)	
$CH_3 + CH_3$	W33	CH_3CH_3	4.6	−323.6					1
	W18		NB	−333.4	None				1
	noW		NB	−338.1					
$CH_3 + NH_2$	W33	CH_3NH_2	NB	−319.2					1
	W18		NB	−316.8	None				1
	noW		NB	−309.1					
$CH_3 + CH_3O$	W33	CH_3OCH_3	3.1	−290.1	$CH_4 + H_2CO$	9.5	−301.9	47.1	1, 3
	W18		NB	−299.5		1.0	−302.7	36.1	2
	noW		NB	−298.3		1.7	−297.5		
$CH_3 + CH_2OH$	W33	CH_3CH_2OH	2.5	−310.0	$CH_4 + H_2CO$	39.0	−258.5	242.0	1, 3(?)
	W18		1.9	−320.4		23.9	−255.1	295.7	1, 3(?)
	noW		NB*	−327.5[a]		9.8	−273.1		
HCO + HCO	W33	CHOCHO	4.1	−268.0	$CO + H_2CO$	4.0	−279.5	28.4	2
	W18		4.0	−260.3		2.7	−272.7	10.8	2
	noW		NB	−275.2[a]		NB	−278.5[a]		
$HCO + CH_3O$	W33	CH_3OCHO	3.5	−351.6	$CO + CH_3OH$	2.0	−322.2	34.6	2
	W18		5.1	−358.5		3.2	−323.4	57.8	2
	noW		NB*	−358.6[a]		NB*[b]	−326.3		
$HCO + CH_2OH$	W33	$CHOCH_2OH$	1.7	−288.6	$CO + CH_3OH$	NB*	−295.8	–	2
	W18		1.6	−286.2		NB*	−290.2	–	2
	noW		NB*	−303.8[a]		NB*[b]	−297.8		
$HCO + CH_3$	W33	CH_3CHO	5.5	−324.5	$CH_4 + CO$	7.2	−328.9	40.0	4
	W18		1.8	−329.5		5.0	−321.5	8.0	1
	noW		NB	−326.1[a]		NB	−340.4[a]		
$HCO + NH_2$	W33	NH_2CHO	2.1	−385.7	$NH_3 + CO$	1.4	−335.0	28.8	2
	W18		3.8	−364.9		4.9	−338.4	7.3	2
	noW		NB	−388.4[a]		NB	−344.0[a]		
$CH_3O + CH_3O$	W33	$(CH_3O)_2$	20.1	−58.3	$CH_3OH + H_2CO$	11.7	−292.3	225.7	4
	W18		10.3	−64.1		15.9	−312.5	212.9	4, 3(?)
	noW		1.8	−75.0		8.1	−284.1		
$CH_2OH + CH_2OH$	W33	$(CH_2OH)_2$	2.6	−299.5	$CH_3OH + H_2CO$	9.0	−245.8	296.2	1
	W18		4.4	−288.7		27.6	−226.3	394.3	1
	noW		10.7	−295.1		6.0	−241.0		

Notes. Col. (1) reports the radical–radical system, and Col. (2) the ice model to which the computations apply, i.e., W33 or W18 ice models or absence of water molecules (noW). Cols. (3)–(5) report the Radical coupling (Rc) product (Col. (3)) with the (ZPE-corrected) activation energy ($\Delta H^{\ddagger}$; Col. (4)) and the reaction energy (ΔH^{reac}; Col. (5)). Cols. (6)–(9) report the direct H-abstraction (dHa) product (Col. (6)) with the (ZPE-corrected) activation energy ($\Delta H^{\ddagger}$; Col. (7)), the reaction energy (ΔH^{reac}; Col. (8)), and the crossover temperature (T_c; see Appendix J; Col. (9)). The last column reports the category to which the reaction belongs (see text), based on the efficiencies computed in Equation (2) (assuming a diffusion-to-desorption barrier ratio of 0.35) and the crossover temperatures: (1) Rc plausible and dHa not plausible/possible; (2) Rc-dHa competition; (3) Rc-dHa competition at low temperatures thanks to tunneling; (4) Rc not plausible, dHa only plausible at low temperatures thanks to tunneling. Energy units are kJ mol^{-1}, temperatures in K. CH_3/HCO and NH_2/HCO values on W18 and W33 were recalculated from those of Enrique-Romero et al. (2019). The main difference is on the dispersion correction used in this work (see also Enrique-Romero et al. 2021). NB* indicates that the reaction has no effective barrier (<1 kJ mol^{-1}), although a transition state was found, which, after correcting for ZPE, goes below the energy of the reactants.
[a] Calculated with respect to the asymptote (i.e., the sum of the energy of both radicals alone).
[b] Regarding the dHa reactions of HCO + CH_3O/CH_2OH in the absence of water molecules, we report those for the dHa1 channel (i.e., HCO transfers its H atom to the partner radical). The dHa2 channels where CH_3O or CH_2OH transfers its H atoms to HCO have higher barriers, of 5.3 and 8.8 kJ mol^{-1}, respectively, similar to CH_3 + CH_3O/CH_2OH.

Please note that Tables 4 and 5 also report the efficiencies and T_{des} of the HCO + CH_3/NH_2 systems. The first one, leading to acetaldehyde, has been fully studied in Enrique-Romero et al. (2020, 2021), while the energetics of the second system, leading to formamide, was presented in Rimola et al. (2018).

Finally, it must be noted that the reported efficiencies are not the same as branching ratios. The latter take into account the rate at which radicals meet on the surface, together with the efficiencies themselves, and provide a perspective of the relative importance of the different reaction channels that two reactants can follow (e.g., Enrique-Romero et al. 2021). On the other hand, the efficiencies tell us what is the probability that two reactants will react in a given reaction site on the surface before one of the two reactants diffuses or ultimately desorbs.

W33 ice ASW model. Table 4 shows that out of the 11 reported systems, nine iCOMs forming reactions have

Table 4
Efficiencies, ϵ, of Radical–Radical Reactions on the W33 ASW Ice Model

System	Fastest Hopper	T_{des} (K)	$T = T_{des}$ Rc Efficiency	$T = T_{des}$ dHa Case 1 Efficiency	$T = T_{des}$ dHa Case 2 Efficiency	$T = 10$ K Rc Efficiency	$T = 10$ K dHa Case 1 Efficiency	$T = 10$ K dHa Case 2 Efficiency
$CH_3 + CH_3$	CH_3	29	0.7	⋯	⋯	1.0	⋯	⋯
$CH_3 + NH_2$	CH_3	29	1.0[a]	⋯	⋯	1.0[a]	⋯	⋯
$CH_3 + CH_3O$	CH_3	29	1.0	0.0	⋯	1.0	0.0	⋯
$CH_3 + CH_2OH$	CH_3	29	1.0	0.0	⋯	1.0	0.0	⋯
HCO + HCO	HCO	60	1.0	1.0	⋯	1.0	1.0	⋯
$HCO + CH_3O$	HCO	60	1.0	1.0	2.9×10^{-3}	1.0	1.0	0.0
$HCO + CH_2OH$	HCO	60	1.0	1.0[a]	[b]	1.0	1.0[a]	[b]
$CH_3O + CH_3O$	CH_3O	77	1.3×10^{-5}	0.9	⋯	0.0	1.0	⋯
$CH_2OH + CH_2OH$	CH_2OH	103	1.0	[b]	[b]	1.0	[b]	[b]
$HCO + CH_3$	CH_3	29	0.1	1.1×10^{-4}	⋯	2.6×10^{-3}	0.0	⋯
$HCO + NH_2$	HCO	60	1.0	1.0	⋯	1.0	1.0	⋯

Notes. They are calculated using Equation (2), setting the temperature to T_{des} and 10 K, respectively, and considering that the diffusion barriers are equal to 0.35 times those of desorption. Note that the quoted values do not take into account quantum tunneling, which could make efficiency larger at very low temperatures.
[a] Barrierless, therefore efficiency is 1 and no crossover temperature can be calculated.
[b] Multiple steps and high barriers, therefore very little efficiency. No crossover temperature is listed, as only the very last step will actually benefit from tunneling.

Table 5
Efficiencies, ϵ, of Radical–Radical Reactions on the W18 ASW Ice Model

System	Fastest Hopper	T_{des} (K)	$T = T_{des}$ Rc Efficiency	$T = T_{des}$ dHa Case 1 Efficiency	$T = T_{des}$ dHa Case 2 Efficiency	$T = 10$ K Rc Efficiency	$T = 10$ K dHa Case 1 Efficiency	$T = 10$ K dHa Case 2 Efficiency
$CH_3 + CH_3$	CH_3	17	1.0[a]	⋯	⋯	1.0[a]	⋯	⋯
$CH_3 + NH_2$	CH_3	17	1.0[a]	⋯	⋯	1.0[a]	⋯	⋯
$CH_3 + CH_3O$	CH_3	17	1.0[a]	1.0	⋯	1.0[a]	1.0	⋯
$CH_3 + CH_2OH$	CH_3	17	1.0	0.0	⋯	1.0	0.0	⋯
HCO + HCO	HCO	42	1.0	1.0	⋯	1.0	1.0	⋯
$HCO + CH_3O$	HCO	42	1.0	1.0	9.6×10^{-4}	1.0	1.0	0.0
$HCO + CH_2OH$	HCO	42	1.0	1.0[a]	0.0	1.0	1.0[a]	0.0
$CH_3O + CH_3O$	CH_3O	53	0.03	0.0	⋯	0.0	0.0	⋯
$CH_2OH + CH_2OH$	CH_2OH	92	1.0	0.0	[b]	1.0	0.0	[b]
$HCO + CH_3$	CH_3	17	1.0	0.0	⋯	1.0	0.0	⋯
$HCO + NH_2$	HCO	42	1.0	1.0	⋯	1.0	1.0	⋯

Notes. They are calculated using Equation (2), setting the temperature to T_{des} and 10 K, respectively, and considering that the diffusion barriers are equal to 0.35 times those of desorption. Note that the quoted values do not take into account quantum tunneling, which could make efficiency larger at very low temperatures.
[a] Barrierless, therefore efficiency is 1 and no crossover temperature can be calculated.
[b] Multiple steps and high barriers, therefore very little efficiency. No crossover temperature is given, as only the very last step will actually benefit from tunneling.

efficiencies close to 1 by the end of the shortest radical residence on the ice surfaces, namely, at temperatures T_{des}, while two (forming dimethyl peroxide and acetaldehyde) have efficiencies less than 0.1. Similarly, out of the nine systems where H-abstraction reactions are possible, five have efficiencies close to 1 at T_{des} (basically those with the form HCO + X → CO + HX, thanks to the low energy barriers involved). On the contrary, the efficiency of four H-abstraction reactions ($CH_3 + CH_3O$, $CH_3 + CH_2OH$, $HCO + CH_3$, $CH_3O + CH_3O$) falls below 1. Notice that the value of the efficiency values are highly sensitive to the E_{diff}/E_{des} ratio value. Changing this ratio from 0.35 to 0.30 yields lower effciencies, while increasing it to 0.40 provides higher efficiency values. In fact, increasing this ratio, one allows the radicals to stay longer in a given binding site, increasing the reaction efficiency. For example, the efficiency of the $CH_3 + CH_3 \rightarrow C_2H_6$ reaction would go

down from 0.7 (using a ratio of 0.35) to ∼0.1 for a ratio of 0.3 and up to ∼1 for a ratio of 0.4. On the same vein, setting the E_{diff}/E_{des} ratio equal to 0.5 makes almost all reactions have an efficiency of 1, due to the longer time that radicals would remain together as a result of the lower diffusion. Changing the temperature at which ε is computed has, in most cases, no effect, indicating that the reaction and diffusion processes are not competitive even at such low temperatures. The exceptions are those reactions that have a small efficiency at T_{des} in Table 4.

W18 ASW ice model. The reaction efficiency calculations were also carried out for the systems on the W18 ice ASW model, where radical mobilities are higher owing to the overall lower binding energies and the simpler reaction mechanisms (usually single step reactions). The results are reported in Table 5. At both T_{des} and 10 K, all iCOMs forming reactions have efficiencies close to 1, except the one from the CH_3O + CH_3O system, which, due to its high barrier, has an efficiency of the order of 10^{-2}. On the contrary, five H-abstraction reactions have efficiencies close to 1, while four have efficiencies close to 0, at both T_{des} and 10 K.

5. Discussion

5.1. iCOM Formation versus H Abstraction

In this work, two radical–radical surface reactions-types have been investigated: radical coupling (Rc) and direct hydrogen abstraction (dHa). The former leads to the formation of iCOMs, while the latter does not lead to an increase in chemical complexity, as the products are as simple as the reactants. Using the binding energies (Table 2), activation energy barriers (Table 3), and the reaction efficiencies ε (Tables 4), here we discuss which radical–radical reaction will likely take place and if there will be a competition between the Rc and dHa channels.

Depending on the values of the efficiencies and the crossover temperature for the Rc and dHa reactions (Tables 4 and 5), we can define four categories:

(1) Rc plausible and dHa not plausible/possible: the reaction will lead to the iCOM with no competition channel.
(2) Rc–dHa competition: both reactions are possible and are in competition.
(3) Rc–dHa competition at low temperatures because of the tunneling taking over in the dHa reactions.
(4) Rc not plausible and dHa only plausible at low temperatures thanks to tunneling: the reaction will not form the iCOM and, except at low temperatures, not even the competing channel will occur.

Based on these reaction categories, here we briefly discuss, in a qualitative manner, which iCOMs are likely to be formed, and in which cases the Rc processes may be in direct competition with the dHa ones.

In three cases (CH_3 + CH_3, CH_3 + NH_2, and CH_2OH + CH_2OH), the only possible product is the iCOM (namely, ethane, methylamine, and ethylene glycol, respectively). We have categorized these reactions as category 1 on both W33 and W18 ASW ice model surfaces given their high efficiencies even at low temperatures ($\varepsilon > 0.7$). In four cases (HCO + HCO, HCO + CH_3O, HCO + CH_2OH, and HCO + NH_2), the formation of the iCOM (glyoxal, methyl formate, glycolaldehyde, and formamide) and the dHa products are likely competing processes on both the W33 and W18 ice models. In practice, all reactions involving HCO (except HCO + CH_3; see Enrique-Romero et al. 2021) have Rc and dHa (of the HCO + X → CO + HX type) as competitive channels. Therefore, while iCOMs can be formed, a significant part of the reactants could be lost via these dHa reactions. In the other two cases (CH_3 + CH_3O and CH_3 +CH_2OH), iCOM formation (dimethyl ether and ethanol) is the dominant process except at low temperature, where H abstraction can take over and become competitive thanks to quantum tunneling.

Finally, in two systems (HCO + CH_3 and CH_2OH + CH_2OH), iCOM formation (acetaldehyde and dimethyl peroxide) is unlikely to occur. This is in agreement with the recent experiments by Gutiérrez-Quintanilla et al. (2021), who did not observe the formation of either acetaldehyde or dimethyl ether despite the presence of the radical reactants.

In summary, assuming that radicals have already diffused and have been encountered in a specific place similar to those represented by our ASW model ices, most iCOMs in the systems studied in this work are likely to be formed on the icy surfaces. However, while ethane, methylamine, and ethylene glycol are the only possible products, glyoxal, methyl formate, glycolaldehyde, formamide, dimethyl ether, and ethanol are likely in competition with the respective H-abstraction products. On the other end, acetaldehyde and dimethyl peroxide do not seem to be likely grain-surface products.

Finally, we caution that this just represents one part of the Langmuir–Hinshelwood reactivity. As discussed also in Enrique-Romero et al. (2021), the binding and diffusion energies are crucial parameters. In this study, we assumed (computed) a single value for the binding energy, but it is now clear that it depends on the site where the species lands (e.g., Bovolenta et al. 2020; Ferrero et al. 2020). Also, as already mentioned, the diffusion energy is poorly known. Since both parameters enter in an exponential way in the computation of the efficiencies, more theoretical studies are necessary to firmly draw a conclusion, which depends on the fraction of sites with low or high binding and diffusion energies. Nonetheless, this study shows that these computations are absolutely necessary in order to have quantitative and reliable astrochemical models.

5.2. Where Do Barriers Come from?

There are two factors affecting the energy barriers of the reactions. The first one is related to the adsorption of the radicals on the surface, i.e., the way they adsorb and the strength of this adsorption. All the studied radicals in this work interact with the water molecules exposed on the ice surfaces via H-bond and dispersion interactions, in which CH_3 and CH_2OH present the weakest and the strongest binding, respectively. Because of these interactions, radical–radical reactions on water-ice surfaces exhibit energy barriers, as the reactions require the breaking of these radical/surface interactions. Remarkably, since the radical/surface interactions dictate the geometries of the adsorbed radicals, these interactions also have repercussions on the structural reorganization of the reactants necessary for the occurrence of the reactions. Take, for example, the dHa channels in which CH_2OH transfers its H atom. CH_2OH interacts with the surface mainly through two strong H bonds involving the –OH group. Accordingly, dHa reactions require a large reorientation, including the breaking of the CH_2–OH/surface H bonds, to proceed with the reaction, which is accompanied by a high energy barrier. The second factor is related to the intrinsic

feasibility of the reactions, that is, how stable against reaction are the biradical systems. To assess this point, we have investigated the reaction in absence of the water cluster, in this way to know the intrinsic energy cost (i.e., without the presence of external agents like the water clusters) of the reactions (see Section 3). Results are shown in Table 3 ("noW" rows), while the structures of the optimized geometries are available at doi:10.5281/zenodo.5723996. We have detected that dHa channels involving either CH_3O or CH_2OH in which they transfer the H atom, irrespective of the other radical, all present energy barriers. This means that the H transfer from these two radicals is intrinsically associated with an energy cost. In contrast, this is not the case for dHa channels in which HCO transfers its H atom, since all these processes are barrierless in absence of the water clusters. Thus, HCO is a better H-atom donor than CH_3O and CH_2OH and, accordingly, dHa channels involving HCO are more favorable than those involving CH_3O and CH_2OH. This is indeed reflected in the energy barriers of the dHa processes on W33/W18, which are lower for cases with HCO than for those with CH_3O or CH_2OH.

For Rc channels in the absence of water molecules, those in which either HCO or CH_3 participates, irrespective of the other radical, are barrierless, indicating that couplings involving these two radicals are largely favorable. This is reflected in the energy barriers on W33/W18, which are in most of the cases very low. In contrast, the Rc channels of $CH_3O + CH_3O$ and $CH_2OH + CH_2OH$ in the absence of water molecules do have energy barriers, showing that these two couplings are intrinsically less favorable than those involving HCO and CH_3. The reason why the $CH_3O + CH_3O$ and $CH_2OH + CH_2OH$ Rc reactions are not barrierless in the absence of an ice surface is the high stability of their biradical van der Waals complexes, i.e., $CH_3O \cdots CH_3O$ and $CH_2OH \cdots CH_2OH$. On the W33/W18 ASW ice models, these van der Waals complexes cannot be formed as a consequence of the interaction with the surface. Indeed, the $CH_2OH + CH_2OH$ Rc reactions on W33/W18 have similar energy barriers to those of HCO + X and CH_3 + X, because the coupling does not require either a strong structural reorganization or the breaking of the CH_2OH/surface interactions, this way rendering the C–C bond formation energetically easy. And for the case of the $CH_3O + CH_3O$ Rc channel on W33/W18, energy barriers are much higher than in the absence of water molecules, due to the energetic cost of breaking the CH_3O/surface interactions and reorienting the radicals to reach the coupling.

5.3. CH_3O and CH_2OH: Who Stays and Who Goes?

CH_3O and CH_2OH radicals are chemical isomers but exhibit different adsorption features and different radical–radical reactivity on ASW surfaces. Both radicals present high binding energies (CH_2OH larger than CH_3O) owing to their capability to establish strong H bonds with the surfaces. Nevertheless, the ways they are established (i.e., atoms involved and number of H bonds formed) are rather different, and this yields differences in their reactivity. CH_2OH interacts with the surface through two strong H bonds involving only the –OH group, this way leaving its C atom (namely, the radical center) unprotected and available to react. This has important consequences for the reactivity of the CH_2OH radical. Indeed, most of the CH_2OH + X reactions (X = CH_2OH, CH_3, and HCO) are Rc plausible, as they present smaller energy barriers and often have fewer reaction steps than dHa. The unique exception is the CH_2OH + HCO reaction, which belongs to the Rc-dHa competition category owing to the intrinsic ease of HCO to transfer its H atom (see above).

In contrast, the unpaired electron in CH_3O is on the O atom, which in turn is the atom through which the radical establishes H bonds with the surface. Because of that, the O atom is blocked toward chemical reactivity, and this is shown by the trends in the CH_3O+X reactions (X = CH_3O, CH_3, and HCO). $CH_3O + CH_3O$ presents very high energy barriers, irrespective of the reaction channel and the ASW model. This is because CH_3O radicals have to reorganize structurally (namely, to break the interactions with the surface) in order to be ready to react. Reactions with CH_3 and HCO show in general Rc-dHa competition, except for the $CH_3 + CH_3O$ case on W33 (Rc plausible) owing to the high dHa barrier (9.5 kJ mol^{-1}) caused by the structural reorientation of CH_3O. Nevertheless, at very low temperatures (<40 K) they could be in competition owing to the increased tunneling probability.

Interestingly, these trends gain relevance if we extrapolate them in the plausible scenario of hydrogenation of CH_2OH and CH_3O, both cases leading to the formation of methanol (CH_3OH). According to our results, an incoming H atom will react easier with CH_2OH than with CH_3O, since the C atom of the former is available while the O atom of the later is blocked. Remarkably, the propensity of the radicals to react is dictated by the geometrical constraints imposed by their interaction with the surface. Thus, in the presence of H atoms, CH_2OH would consume better than CH_3O, which could partly explain why CH_3O is detected and CH_2OH is not (e.g., Cernicharo et al. 2012).

5.4. Influence of the Water-ice Surface Model

The W33 ASW ice surface model presents a ∼6 Å wide cavity where both radicals can be adsorbed. In contrast, the W18 model does not exhibit a cavity, resembling instead a rather flat surface. As shown in Section 4.1, the binding energies on W33 (i.e., adsorption on the cavity) are larger (by a 12%–76%) than on W18, due to the larger number of radical/surface interactions formed on the former cluster model.

These effects are particularly important in those reactions in which the CH_3 radical participates. Indeed, in different reactions on W33, CH_3 is engaged by two weakly H bonds, this way either hampering its motion toward the other radical (hence disfavoring Rc channels) or inhibiting its capability to receive an H atom from the other radical (hence disfavoring dHa channels; see Figure 3). Indeed, the average energy barrier for Rc reactions involving $CH_3 + X \rightarrow X–CH_3$ on W33 is 3.1 kJ mol^{-1}. In contrast, on W18, CH_3 adsorbs essentially through dispersion forces, and accordingly it is relatively free to translate/rotate to favor the Rc and dHa channels, so that CH_3 + X Rc reactions have a barrier of 0.7 kJ mol^{-1} on average.

For the other radicals, the water-ice surface morphology does not seem to affect the activation energy barriers in a systematic way. These are indeed more complex cases than the CH_3 ones, since the reacting radicals can adsorb in different ways, establish different radical/surface interactions with different efficiencies, and require different structural reorganizations to react. Yet we find that HCO + X → X–CHO Rc reactions have average barriers of 3.4/3.3 kJ mol^{-1} on W33/W18 and average dHa HCO + X → CO + HX reaction energy barriers of 2.9/3.2 kJ mol^{-1} on W33/W18 (see Figure 4).

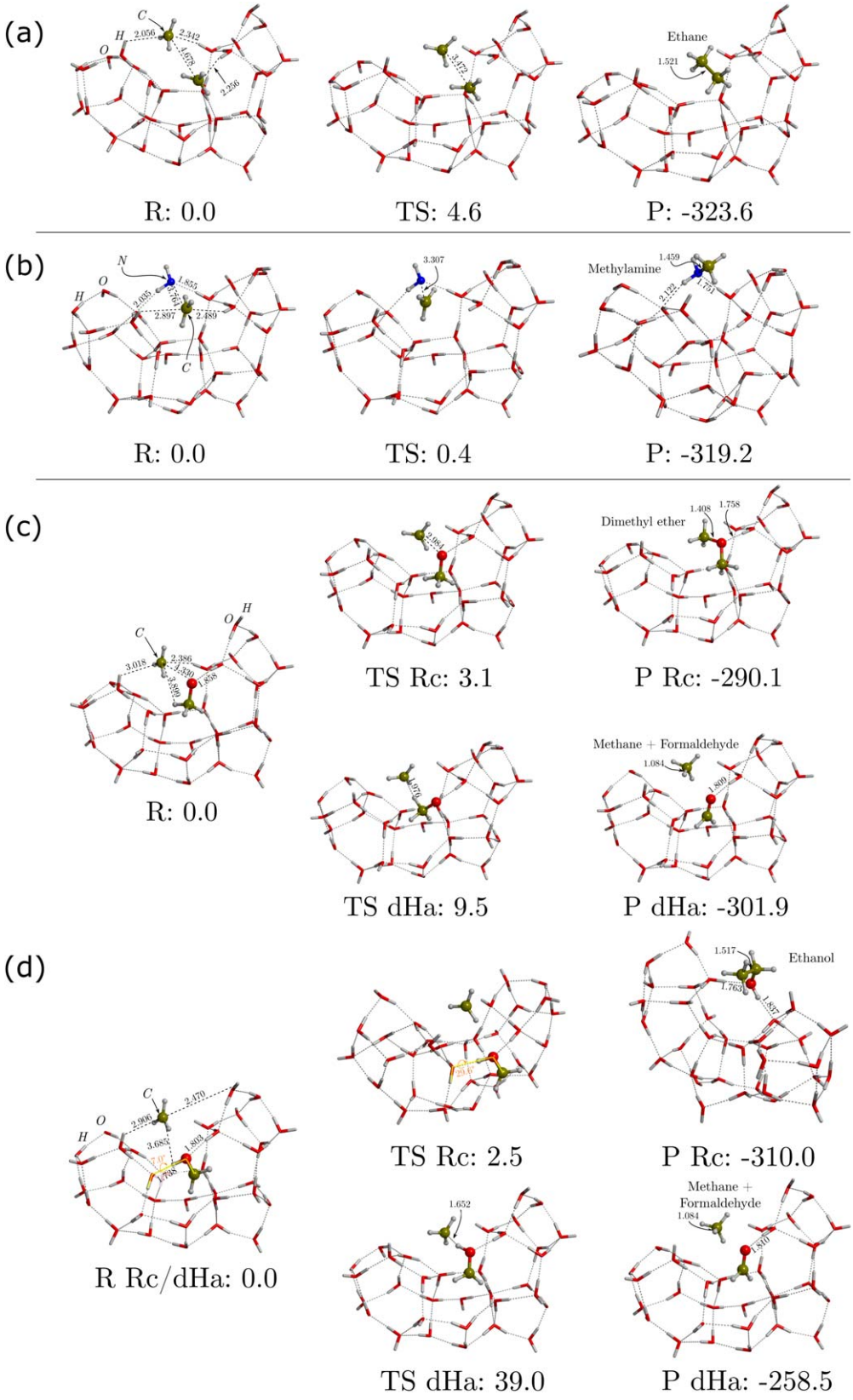

Figure 3. Relative ZPE-corrected potential energies of the stationary points for (a) CH_3/CH_3, (b) CH_3/NH_2, (c) CH_3/CH_3O, and (d) $CH_3/CH{-}2OH$ on W33-cav fully optimized at the BHLYP-D3(BJ)/6-31+G(d,p) theory level. DFT energies were further refined at the BHLYP-D3(BJ)/6-311++G(2df,2pd) theory level. Energy units are in kJ mol^{-1} and distances in angstroms.

(The complete figure set (9 images) is available.)

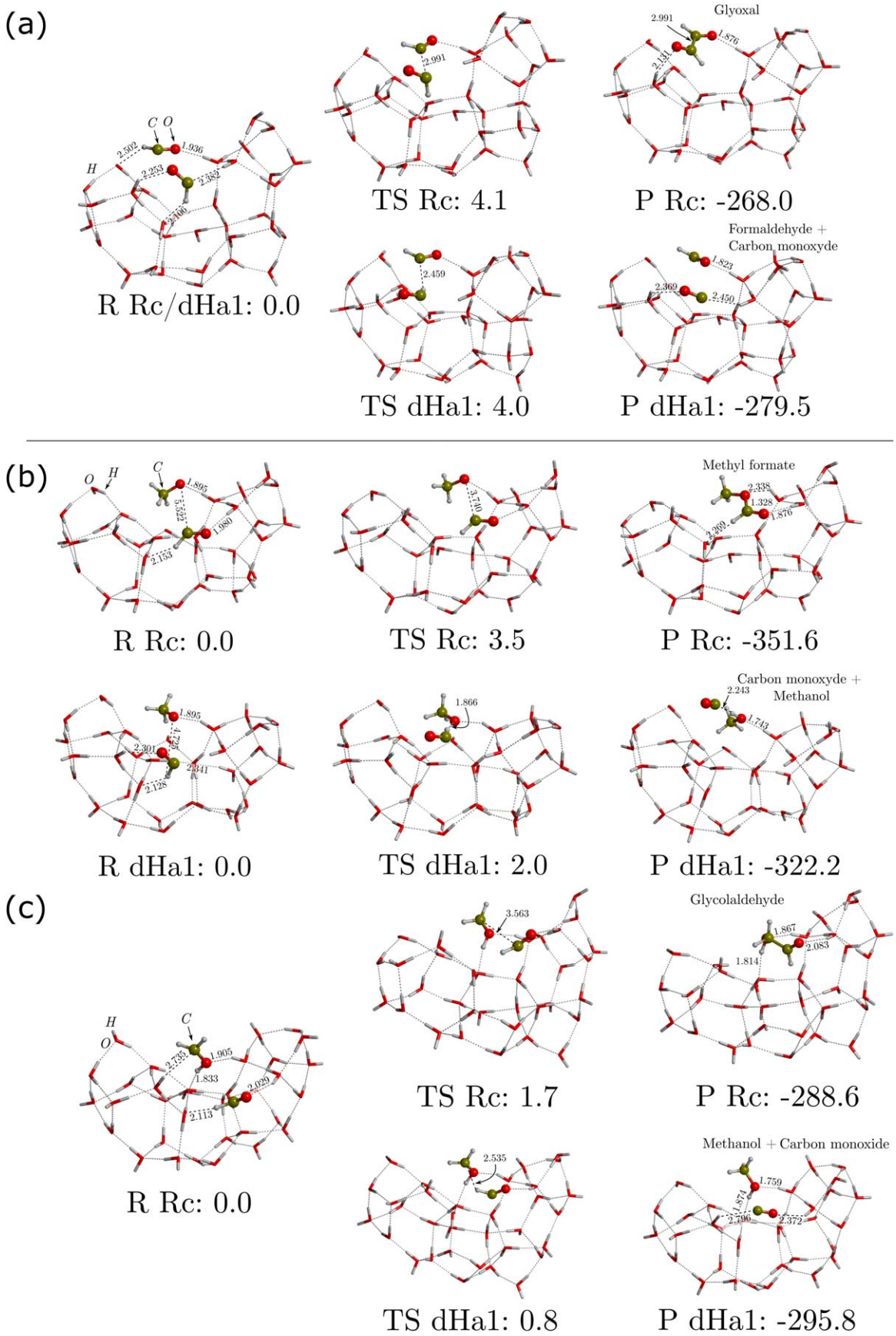

Figure 4. Relative ZPE-corrected potential energies of the stationary points for (a) HCO/HCO, (b) HCO/CH_3O, and (c) HCO/CH_2OH on W33-cav fully optimized at the BHLYP-D3(BJ)/6-31+G(d,p) theory level. DFT energies were further refined at the BHLYP-D3(BJ)/6-311++G(2df,2pd) theory level. Energy units are in kJ mol^{-1} and distances in angstroms.

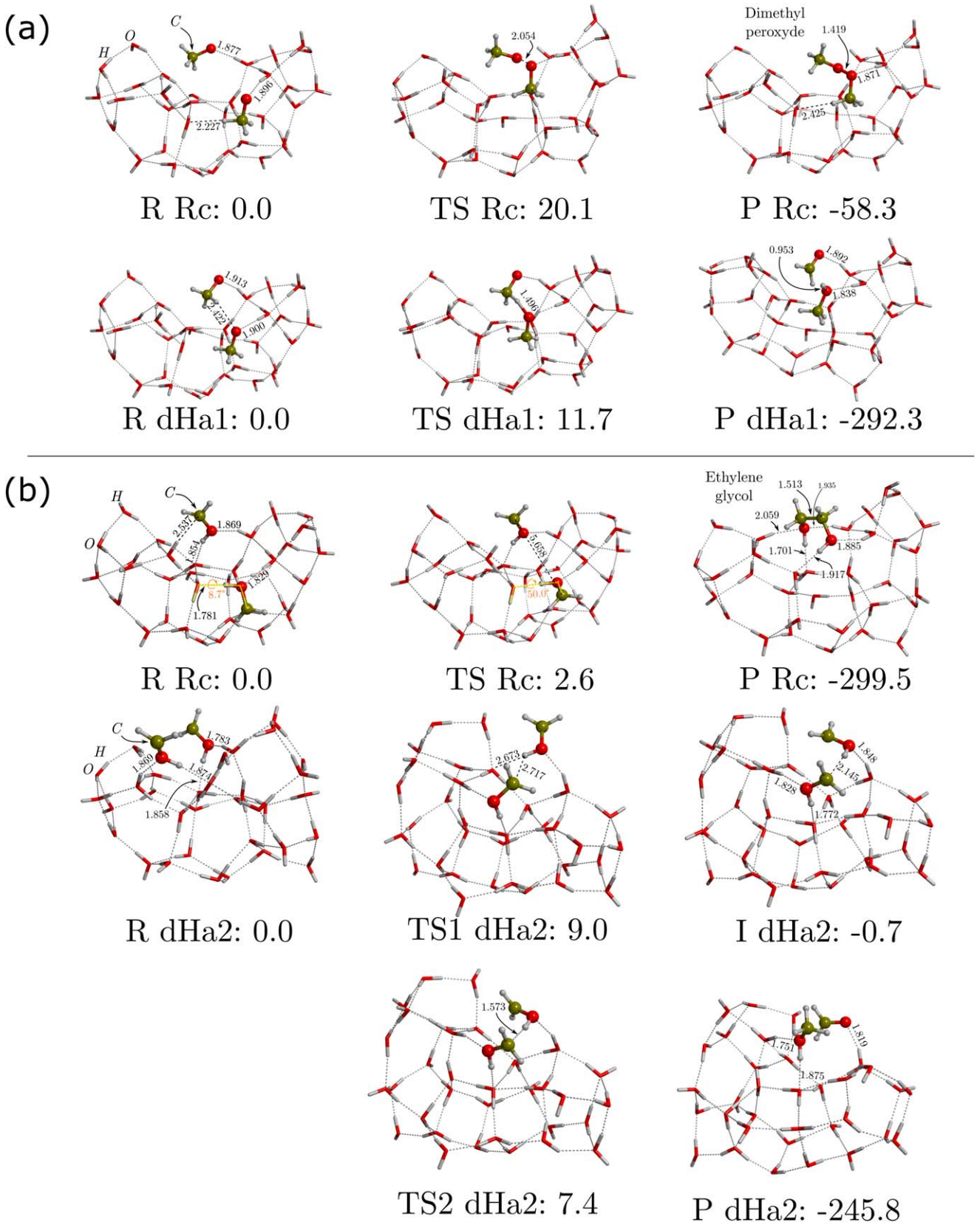

Figure 5. Relative ZPE-corrected potential energies of the stationary points for (a) CH_3O/CH_3O and (b) CH_2OH/CH_2OH on W33-cav fully optimized at the BHLYP-D3(BJ)/6-31+G(d,p) theory level. DFT energies were further refined at the BHLYP-D3(BJ)/6-311++G(2df,2pd) theory level. Energy units are in kJ mol^{-1} and distances in angstroms.

(The complete figure set (5 images) is available.)

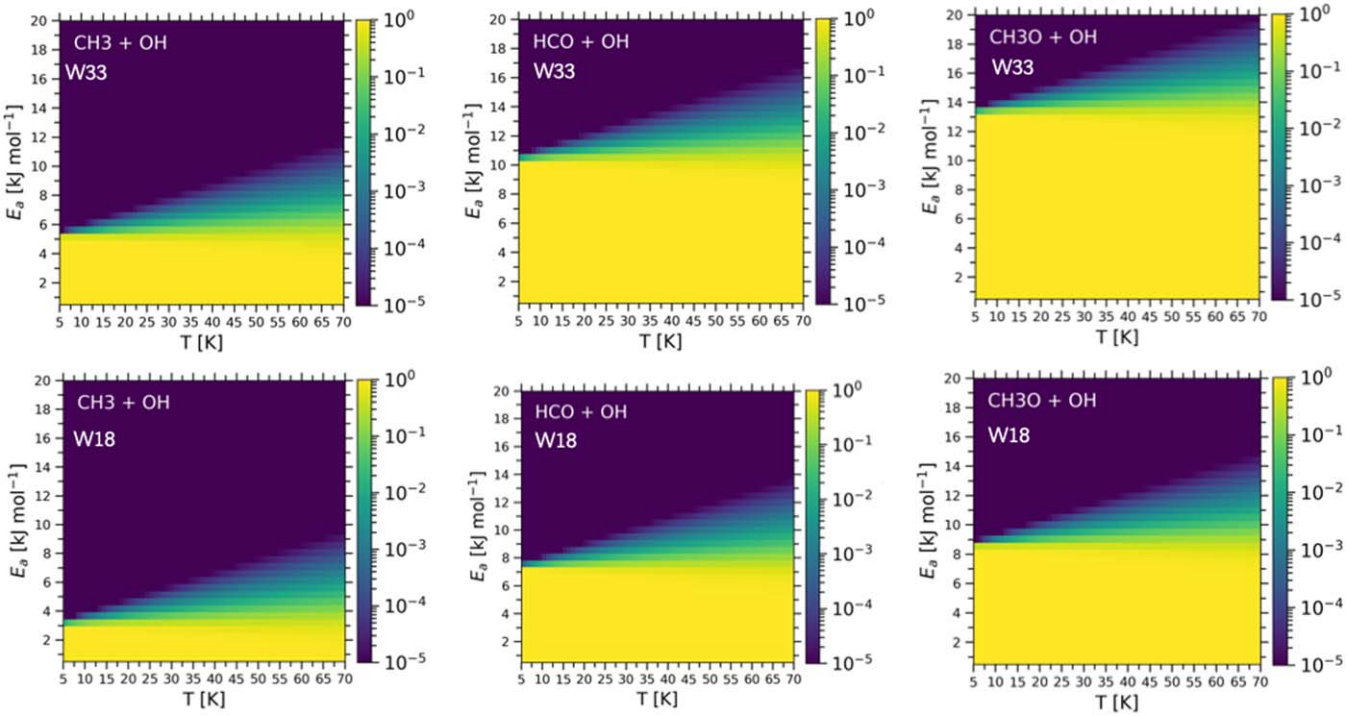

Figure 6. Reaction efficiencies on W33 (top panels) and W18 (bottom panels) as a function of the activation energy and temperature of a subset of the radical–radical systems in Garrod et al. (2008) not explicitly studied in this work and for which we guess their efficiency (see text). These calculations do not include tunneling effects.

Finally, some words related to our cluster models deserve to be mentioned. The first aspect is that they are rather small, although they are capable of hosting two small radicals on the surface. However, the limited sizes infer that, in the initial states, the reacting radicals are in close proximity. Thus, the predicted energy barriers concern only the chemical reactions between the radicals and not other surface phenomena like diffusion. In real systems, the two radicals will be likely separated by longer distances, and thus diffusion is necessary. The second aspect is that the clusters composition is purely water, while actual ice mantles will contain other species. Thus, the interaction of the radicals with the surface can be different, affecting the diffusion, the reaction energies, and the survival of the radicals against hydrogenation reactions. Therefore, the energy barriers reported in this work are constrained within these two aspects, assuming that ice composition plus extensive radical diffusion are actually needed for a more realistic modeling.

5.5. Predictions for Other Radical–Radical Systems

There are several other radical–radical systems proposed in the literature (e.g., Garrod et al. 2008) that we did not study in the present work, for example, OH/NH + X (X = CH_3, HCO, OH, NH, NH_2, CH_3O, CH_2OH), NH_2 + Y (Y = NH_2, CH_3O, CH_2OH), and CH_3O + CH_2OH. However, studying such systems is a highly time-consuming task. Therefore, here we propose to use the trends for the studied reactions and the classification in categories 1–4 discussed in Section 5.1 as a predictive tool to estimate a likely category of these other radical–radical reactions.

As for the reactions studied in this work, the category classification is based on the reaction efficiency (Section 3.4), which depends on the reaction energy barrier, radical binding, and diffusion energies. In order to guess the reaction category, we apply the following set of considerations:

1. If the reaction mechanism only involves translations/rotations without the need to break the radical/surface interactions (e.g., the Rc reactions on W18 of the type CH_3 + X with X = CH_3, NH_2, HCO, CH_3O, CH_2OH), then we estimate the energy barriers to be low (lower than about 4 kJ mol^{-1}).
2. If the reaction involves the breaking of strong radical/surface interactions (e.g., Rc and dHa for CH_3O + CH_3O), or the translation of a radical somehow trapped by the ice (e.g., CH_3 in CH_3 + CH_3/CH_3O on W33), then we estimate the energy barriers to be high (higher than about 10 kJ mol^{-1}).
3. For dHa channels only, if the reaction involves the cleavage of intrinsically stable chemical bonds (e.g., the CH_2O–H bond), then we consider the energy barriers to be high ($\geqslant$10 kJ mol^{-1}). If the reaction involves the opposite situation (e.g., the H–CO bond), then we consider the energy barriers to be low ($\leqslant$4 kJ mol^{-1}).

Given the fundamental role that the binding energies play in such surface reactions, we have calculated the binding energies of NH (in its triplet electronic ground state) and OH radicals on the water-ice clusters.

They are 13.0 and 24.2 kJ mol^{-1} on the W18 model and 32.5 and 44.7 kJ mol^{-1} on the cavity of the W33 model, for NH and OH, respectively (see Figure C1 in Appendix C). Thus, NH has a binding energy that lies between HCO and NH_2, while OH is almost the same as NH_2. With this information, we obtain the E_a- and T-dependent efficiencies (of either Rc or dHa reactions) for each system with OH + X, NH + X (X = CH_3, HCO, OH, NH_2, CH_3O, CH_2OH), NH_2 + Y (Y = NH_2, CH_3O, CH_2OH), and CH_3O + CH_2OH. Figure 6 contains a subset of them:

OH + CH_3, HCO, CH_3O on both W33 and W18. The figures relative to the other systems are available in Appendix I.

It can be rapidly noticed that there is a limit under which the efficiencies take values of unity; this is the point at which the reaction energy barriers coincide with the value of the diffusion barrier of the fastest hopper from each couple (i.e., $E_{diff} = 0.35 \times E_{des}$), and it is surface and radical dependent. Of course, the higher the binding energy (CH_3 < HCO < CH_3O < OH < CH_2OH), the higher this limit, meaning that for activation energy values below this threshold radicals have enough time to react before they separate owing to thermal hopping. On the contrary, above this energetic limit, the dependence on temperature becomes more and more important, so that at higher temperatures higher efficiencies are obtained. Eventually, for sufficiently high activation energies, the reactivity between two radicals becomes inefficient.

While these plots are very informative, they lack three key points in the Langmuir–Hinshelwood-like surface reactions: (i) the temperature limit after which radicals will certainly not be available on the surface anymore (e.g., a theoretical limit can be set at the "desorption temperature," see Section 3.4 for more details, while it could also be the point at which some of the two radicals have been consumed); (ii) the effects of quantum tunneling, which may be important for direct H-abstraction reactions, so that the rate constants related to the activation energy barriers become less dependent on temperature; and, finally, (iii) the meeting rates, which will modulate the efficiency according to the meeting probability of radicals on the grain surfaces. Such effects are only attainable by more detailed, dedicated modeling.

In summary, in addition to the three considerations from above, one must also consider that the higher the binding energies of the radical couple, the higher the range of activation energy barriers that the reaction can have in order to present high efficiencies, at the expense of a lower meeting rate.

With this information, and bearing in mind the three above considerations, we propose the guessed reactivity properties for each one of these systems in the following paragraphs.

5.5.1. Radical Coupling Reactions

OH + X: (X = CH_3, HCO, OH, NH, NH_2, CH_3O, CH_2OH). OH has a high binding energy on W33 (44.7 kJ mol^{-1}) and an intermediate one on W18 (24.2 kJ mol^{-1}). Therefore, its diffusion barrier is rather high. For reactions with a radical X that have small diffusion barriers, like CH_3 or NH (the latter only on W18), reactions will take place only if they have small activation energy barriers. For such low binding energy radicals, this might hold as long as they do not experience trapping. On the other hand, if the radical X has also a high diffusion barrier, the reaction efficiencies will be unity even for relatively high activation energy barriers. There might be two cases where reactions could have very high reaction energies, and as a consequence low efficiencies, X = OH/CH_3O, since they both have their radical atom (oxygen) establishing H-bonding.

NH + X: (X = CH_3, HCO, OH, NH, NH_2, CH_3O, CH_2OH). NH has an intermediate to low binding energy depending on the surface environment (13.0 kJ mol^{-1} on W18 and 32.5 kJ mol^{-1} on W33). Therefore, one would expect low energy activation energy barriers on flat surfaces where NH can easily reorient, meaning high efficiencies. On the contrary, the high binding energy on W33 renders NH + X reactions efficient as long as the barrier is not very high, a scenario that is likely not given by any of the possible X radicals based on the experience with the systems we have studied.

NH_2 + X: (X = NH_2, CH_3O, CH_2OH). The NH_2 radical sports high binding energy regardless of the surface environment. Therefore, reactions with other radicals need to have very high energy barriers in order to have low efficiencies. Hence, we expect high efficiencies for any radical X.

CH_3O + CH_2OH. Given the special binding structure of CH_2OH with its C atom free from surface interaction, we expect these reactions to have high efficiencies, also given their high binding energies.

5.5.2. Direct H-abstraction Reactions

From the list of reactions, only HCO, CH_3O, and CH_2OH can donate an H atom. From our experience with the systems in Table 3, we know that HCO is a very good H donor, while CH_3O and CH_2OH are not. Reactions where HCO is the H donor will most likely sport competition between Rc and dHa channels, while tunneling effects will be much more important for reactions where CH_3O is the H donor. Regarding CH_2OH, its high stability makes energy barriers high and mechanisms more complex, likely with many energetic reorientation steps. Therefore, overall it is expected to be a nonefficient process.

6. Conclusions

In this work, we have carried out DFT computations of the reactions on icy surfaces between nine radical–radical systems, postulated to lead to the formation of iCOMs by several astrochemical models based on the Garrod & Herbst (2006) scheme. The set of studied systems are HCO + X and CH_3 + X, where X is equal to CH_3, HCO, NH_2, CH_2OH, and CH_3O, plus the systems CH_3O + CH_3O and CH_2OH + CH_2OH. We considered both the combination between radicals, leading to the iCOM, and the H abstraction from one of them, leading to simpler molecules.

In order to simulate the interstellar icy surfaces, we employed two ice cluster models made of 18 and 33 water molecules (W18 and W33, respectively), which we tested in previous works (Rimola et al. 2014; Enrique-Romero et al. 2019, 2021). The W33 ice model presents a cavity structure, which likely makes it a better representation of interstellar ices than the W18 ice model, which only possesses a rather flat surface because of its limited size. Therefore, in the following, we will only report the conclusions based on the results obtained with the W33 model.

We computed the binding energy of the involved radicals and, for all the possible reactions between the nine radical–radical systems, the reaction energy barriers. We also computed the diffusion energy of each radical, assuming that it is 0.35 times the binding energy. Then, using the definition of reaction efficiency that takes into account the reaction activation energy barrier, as well as the radical diffusion and desorption timescales (Enrique-Romero et al. 2021), we provided a rough estimate of the reaction efficiency of each reaction using the Eyring equation approximation. The computed reaction efficiencies allow us to predict which reactions will lead to iCOMs or to a competition with the H-abstraction channels, or to nothing.

The main conclusions of this work are the following:

(1) Radical–radical reactions on icy surfaces are not straightforward or barrierless in most of the studied systems. Very often, we find that two channels, radical coupling and H abstraction, are in competition. In a few cases, we find that no reaction can occur between the two radicals. Specifically:

(i) Ethane (C_2H_6), methylamine (CH_3NH_2), and ethylene glycol (CH_2OHCH_2OH) are the only products of their respective radical–radical reactions.

(ii) The formation of glyoxal (HCOCHO), formamide (NH_2CHO), methyl formate (CH_3OCHO), and glycolaldehyde (CH_2OHCHO) is in competition with the H-abstraction products (CO + H_2CO, NH_3 + CO, CH_3OH + CO, and CH_3OH + CO, respectively). Very likely, the branching ratio is 1:1, thanks to the capacity of HCO to become an H donor in the H-abstraction reactions.

(iii) Acetaldehyde (CH_3CHO) and dimethyl peroxide (CH_3OOCH_3) are unlikely to be formed.

(2) The effect of the surface structure on the reaction output is best represented by the different binding energies on the two ice models. On the cavity structure of the W33 model, the binding energies are ∼10%–80% higher than on the W18 model, due to the larger number/efficiency of intermolecular interactions. This effect is higher for weakly bound species like CH_3, evidencing its capacity to get trapped. Nevertheless, the same trend on the binding energy of the different radicals is observed on both ice models: CH_3 < HCO < NH_2 < CH_3O < CH_2OH.

In addition, some radicals present features worth emphasizing.

(3) CH_3 is usually a very reactive species owing to its low binding energy (in many cases its reaction mechanisms comprise a low-energy torsion), although there are some exceptions where the mobility of CH_3 is much restricted by the cavity in W33, so that the activation energy barriers can rise up to ∼7 kJ mol^{-1}.

(4) CH_2OH presents an interesting binding pattern to the ice surface, which makes its C atom very reactive. The strong interaction of its OH group with the water molecules of the surface fixes its adsorption geometry, leaving the C atom unprotected and highly reactive. We predict that its reactivity with other radicals (with very low energy barriers) and especially with atomic hydrogen will be a major destruction route for this radical on the icy surfaces.

(5) CH_3O has its radical electron on the O atom, which in turn establishes H bonds with the surface water molecules. This makes this radical slightly less reactive than expected, and therefore high energy barriers appear for the CH_3O + CH_3O reactions. On the other hand, CH_3O can still perform direct H-abstraction reactions as a donor in other situations. However, the likely high reaction energy barriers, due to its intrinsic H–C bond stability (and for the cavity, the higher number of intermolecular interactions), suggest that the H-abstraction reactions are efficient only when considering quantum tunneling effects.

(6) Here we have studied in detail only a subset of radical–radical reactions present in the Garrod et al. (2008) scheme. For the systems involving the same set of radicals investigated in this work (CH_3, HCO, NH_2, CH_2OH, CH_3O) and, additionally, those involving OH and NH, we have discussed the possible outcomes, based on what we learned from the in-depth studied systems.

As conclusive remarks, we emphasize again that the assumption of the radical–radical combination leading exclusively and always to iCOM is far from correct, and that dedicated studies on each radical–radical system are mandatory to assess the outcome of its possible reactions. Also, the present study uses simplistic models of the ice structure, as well as a very limited number of binding and reaction sites. More realistic computations should include larger icy grains, as well as molecular dynamics simulations involving the encountering plus the reaction of the two radicals, probably possible in the near future thanks to the fast increase of high-performance supercomputing facilities. In conclusion, our study probably has just scratched the surface of the surface chemistry on the icy interstellar grains.

This project has received funding within the European Union's Horizon 2020 research and innovation program from the European Research Council (ERC) for the projects "The Dawn of Organic Chemistry" (DOC), grant agreement No. 741002, and "Quantum Chemistry on Interstellar Grains" (QUANTUMGRAIN), grant agreement No. 865657, and from the Marie Sklodowska-Curie for the project "Astro-Chemical Origins" (ACO), grant agreement No. 811312. A.R. is indebted to the "Ramón y Cajal" program. MINECO (project CTQ2017-89132-P) and DIUE (project 2017SGR1323) are acknowledged. Finally, we thank Prof. Gretobape for fruitful and stimulating discussions.

Most of the quantum chemistry calculations presented in this paper were performed using the GRICAD infrastructure (https://gricad.univ-grenoble-alpes.fr), which is partly supported by the Equip@Meso project (reference ANR-10-EQPX-29-01) of the program Investissements d'Avenir supervised by the Agence Nationale pour la Recherche. Additionally this work was granted access to the HPC resources of IDRIS under the allocation 2019-A0060810797 attributed by GENCI (Grand Equipement National de Calcul Intensif).

We thank Ms. Berta Martínez-Bachs for sharing with us the binding energy values of NH on amorphous water ices.

Appendix A
Radical–Water Interactions

In order to trace the origin of CH_2OH and CH_3O binding energies, we have run optimizations at the BHLYP-D3-BJ/6-311++G(2df,2pd) level and single-point calculations at the CCSD(T)/aug-cc-pVTZ level, similarly to what we did for CH_3, HCO, and NH_2 in Enrique-Romero et al. (2019). For the last three, the main differences are the bond distances (due to the change of DFT method), with minor changes in the interaction energies, smaller than 1 kJ mol^{-1} (comparing the new values to those computed at the BHLYP-D3/6-311++G(2df,2pd)//B3LYP-D3/6-311++G(2df,2pd) level), and the NH–H ⋯ OH_2 geometry from Enrique-Romero et al. (2019) evolves into the NH_2 ⋯ H_2O case shown in Figure A1(d) during optimization. Regarding the two new radicals, CH_3O mainly interacts with the water molecules via a strong H bond on its O atom, while CH_2OH can interact via two strong H bonds on the –OH group, one as an H donor and another as an H acceptor. The resulting geometries and energetics are shown in Figure A1, with the correlation between their ZPE and BSSE noncorrected binding energies in Figure A2. It is worth mentioning that different initial radical–water orientations were tried for CH_3O and CH_2OH, which, after optimization, converged to the ones in Figure A1. All in all, the differences between DFT and CCSD(T) values, i.e., below 2.2 kJ mol^{-1}, correspond to the NH_2 ⋯ H_2O case (Figure A1(d)).

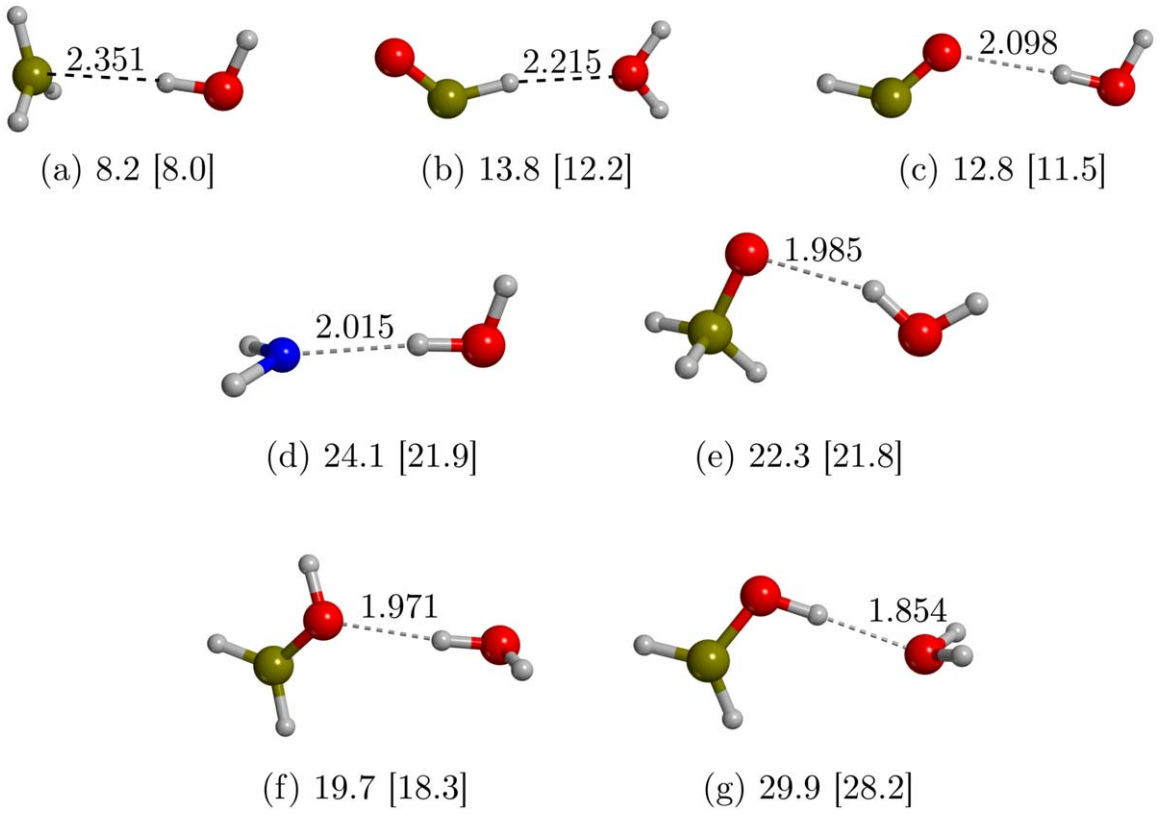

Figure A1. ZPE and BSSE noncorrected binding energies of (a) CH_3, (b, c) HCO, (d) NH_2, (e) CH_3O, and (f), (g) CH_2OH with a single water molecule at BHLYP-D3 (BJ)/6-311++G(2df,2pd) and CCSD(T)/aug-cc-pVTZ//BHLYP-D3(BJ)/6-311++G(2df,2pd) in brackets. Distances in angstroms.

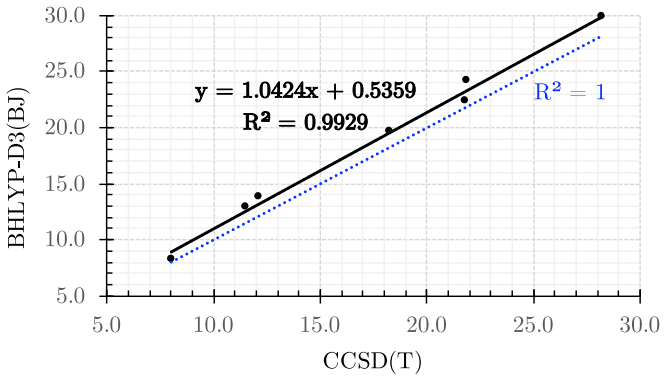

Figure A2. Correlation between ZPE and BSSE noncorrected binding energies of the radicals in Figure A1. Shown are BHLYP-D3(BJ)/6-311++G(2df,2pd) and CCSD(T)/aug-cc-pVTZ//BHLYP-D3(BJ)/6-311++G(2df,2pd) (black filled points) with their trend line and, for the sake of comparison, the line corresponding to a perfect correlation with CCSD(T) data.

Appendix B
Adsorption Geometries on W18

In Figure B1 we report the adsorption geometries of five studied radicals on top of the W18 ice model.

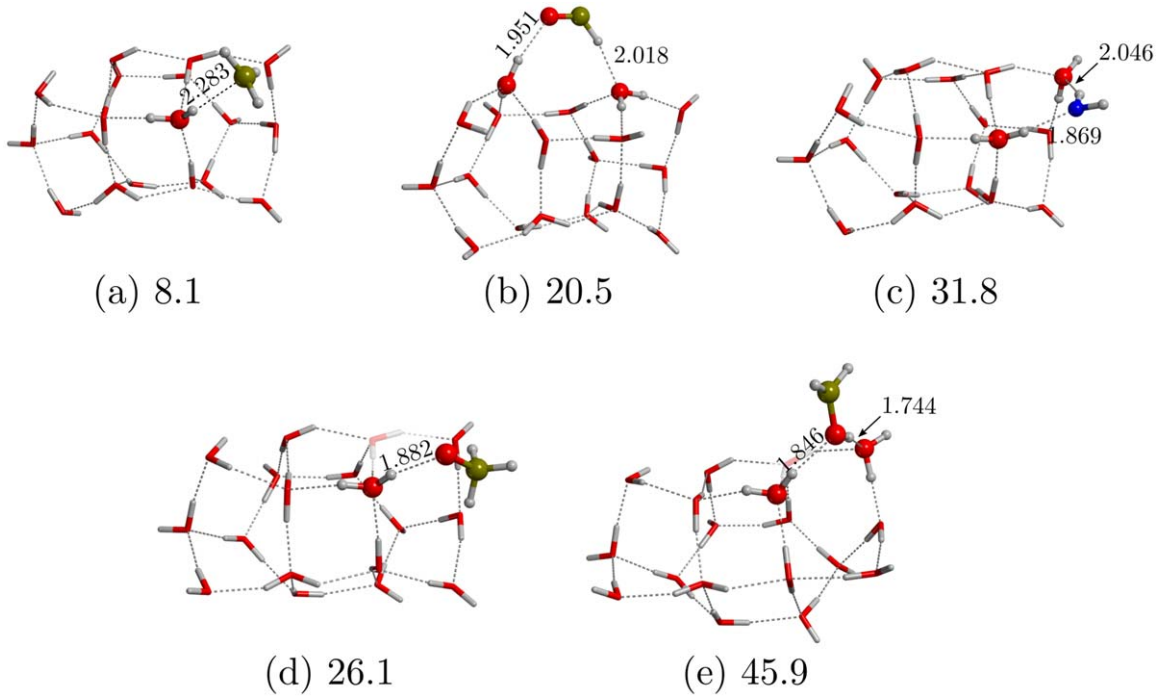

Figure B1. Geometries of the five studied radicals, (a) CH_3, (b) HCO, (c) NH_2, (d) CH_3O, and (e) CH_2H, adsorbed on W18 fully optimized at the UBHLYP-D3(BJ)/6-31+G(d,p) theory level. Energy values in kJ mol^{-1} are those refined at the UBHLYP-D3(BJ)/6-311++G(2df,2pd) level with the ZPE (at the 6-31+G(d,p) level) and BSSE corrections. Distances in angstroms.

Appendix C
Adsorption Geometries of NH and OH on W18 and W33

We have calculated the binding energies of NH (ground triplet electronic state) and OH (doublet electronic state) radicals following the same methodology as for the other radicals in this work. As can be seen from Figure C1, we find again that the binding energies on the W18 ASW ice model, 13.0 and 24.2 kJ mol^{-1} for NH and OH, respectively, are roughly half those on the cavity of W33, 32.5 and 44.7 kJ mol^{-1} for NH and OH, respectively. These values are in good agreement with those in the literature. There are several works reporting the binding energy for OH on water surfaces: Sameera et al. (2017) report a range of binding energies in between 19.3 and 64.6 kJ mol^{-1} on top of a crystalline ice structure, Wakelam et al. (2017) recommend a value of 38.2 kJ mol^{-1} for astrochemical models, and, most recently, Ferrero et al. (2020) report a range in between 12.9 and 44.2 kJ mol^{-1} on amorphous water ice. On the other hand, for NH Wakelam et al. (2017) recommend a value of 21.6 kJ mol^{-1}, which lies in between the values we report for this nitrene. On the other hand, Martínez-Bachs et al. (2020) reported a binding energy of 35.1 kJ mol^{-1} on top of a crystalline water-ice surface. On top of an ASW ice surface, the binding energies cover a wider range, from ∼11 to 45 kJ mol^{-1} (B. Martinez-Bachs, private communication), centered at around 20 kJ mol^{-1}, so that our binding-energy values are well within the limits and close to this central value.

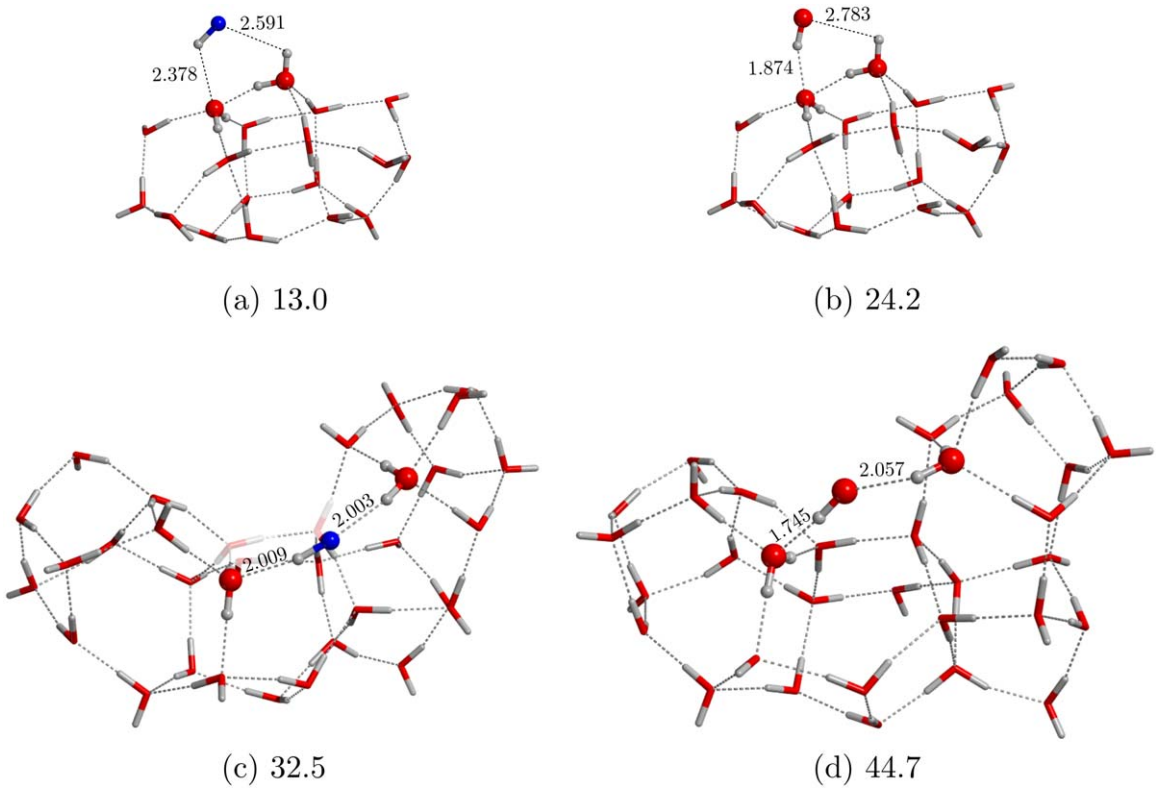

Figure C1. Geometries of NH (in its ground triplet electronic state) and OH (doublet electronic state) on (a, b) W18 and on (c, d) the cavity of W33. These geometries were fully optimized at the UBHLYP-D3(BJ)/6-31+G(d,p) theory level. Energy values in kJ mol^{-1} are those refined at the UBHLYP-D3(BJ)/6-311++G(2df,2pd) level with the ZPE (at the 6-31+G(d,p) level) and BSSE corrections. Distances in angstroms.

Appendix D
Components of the Binding Energies

In Table 6 we report the components of the binding energies. Recall that we define $\Delta E_{\rm bind} = -\Delta E_{\rm ads}$.

Table 6
Components of the Adsorption Energies

W18	$\Delta U_{\rm ads}$	$\Delta D_{\rm ads}$	ΔZPE	BSSE
CH_3	−9.5	−6.7	7.3	0.8
HCO	−26.1	−2.8	6.2	2.3
NH_2	−40.0	−7.2	13.2	2.2
CH_3O	−26.8	−8.4	6.6	2.4
CH_2OH	−50.1	−7.0	8.0	3.2
NH	−14.5	−4.0	4.4	1.1
OH	−28.7	−3.7	6.0	2.2
W33-cav	$\Delta U_{\rm ads}$	$\Delta D_{\rm ads}$	ΔZPE	BSSE
CH_3	−15.3	−0.5	0.5	1.1
HCO	−28.6	−5.0	1.7	2.4
NH_2	−51.3	−2.8	7.0	2.7
CH_3O	−35.8	−14.9	8.9	3.7
CH_2OH	−38.6	−26.3	9.3	4.4
NH	−35.5	−10.3	10.8	2.5
OH	−49.3	−10.1	11.4	3.4

Note. We remind the reader that $\Delta E_{\rm ads} = -\Delta E_{\rm BE}$. U are pure DFT energies, D are dispersion corrections, ZPE are zero-point energies, and BSSE are the basis set superposition error energies. Energy units are kJ mol^{-1}.

Appendix E
Radical–Radical Reaction Energetics

Table 7 shows activation and reaction enthalpies (at $T = 0$) of each radical–radical reactions.

Table 7
Energetics of the Investigated Radical–Radical Reactions on W18 (Left) and W33 (Right)

X+Y···W18	RX	Step No.	$\Delta H^{\ddagger}$	ΔH_{rx}
$CH_2OH + CH_2OH$	Rc		4.4	−288.7
	dHa1		39.1	−223.7
	dHa2	1	20.6	14.9
	dHa2	2	27.6	−226.3
$CH_3O + CH_3O$	Rc		10.3	−64.1
	dHa1		15.9	−312.5
	dHa2		18.2	−296.0
$CH_3 + CH_2OH$	Rc		1.9	−320.4
	dHa	1	23.9	24.2
	dHa	2	32.2	−255.1
$CH_3 + CH_3$	Rc		−0.1	−333.4
$CH_3 + CH_3O$	Rc		0.2	−299.5
	dHa		1.0	−302.7
$CH_3 + NH_2$	Rc		1.6	−316.8
$HCO + CH_2OH$	Rc		1.6	−286.2
	dHa1		−0.6	−290.2
	dHa2		30.7	−182.9
$HCO + CH_3O$	Rc		5.1	−358.5
	dHa1		3.2	−323.4
	dHa2		9.6	−246.3
HCO + HCO	Rc		4.0	−260.3
	dHa1		2.7	−272.7
	dHa2		8.3	−273.3
X+Y···W33	RX	Step No.	$\Delta H^{\ddagger}$	ΔH_{rx}
$CH_2OH + CH_2OH$	Rc		2.6	−299.5
	dHa1	1	1.4	−10.2
	dHa1	2	11.6	7.2
	dHa1	3	9.1	8.0
	dHa1	4	24.9	25.4
	dHa1	5	29.1	−218.3
	dHa2	1	9.0	−0.7
	dHa2	2	7.4	−245.8
$CH_3O + CH_3O$	Rc		20.1	−58.3
	dHa1		11.7	−292.3
	dHa2		21.2	−298.6
$CH_3 + CH_2OH$	Rc	1	2.5	0.5
	Rc	2	0.4	−310.0
	dHa		39.0	−258.5
$CH_3 + CH_3$	Rc		4.6	−323.6
$CH_3 + CH_3O$	Rc		3.1	−290.1
	dHa		9.5	−301.9
$CH_3 + NH_2$	Rc		0.4	−319.2
$HCO + CH_2OH$	Rc		1.7	−288.6
	dHa1		0.8	−295.8

Table 7
(Continued)

X+Y···W33	RX	Step No.	$\Delta H^{\ddagger}$	ΔH_{rx}
	dHa2	1	10.2	10.4
	dHa2	2	18.4	−228.6
$HCO + CH_3O$	Rc		3.5	−351.6
	dHa1		2.0	−322.2
	dHa2		13.2	−242.4
HCO + HCO	Rc		4.1	−268.0
	dHa1		4.0	−279.5

Note. DFT and dispersion energies were calculated at the BHLYP-D3(BJ)/6-311++G(2df,2pd) level, while ZPE corrections were calculated at the BHLYP-D3(BJ)/6-31+G(d,p) level. Col. (2) shows the reaction type, and for dHa whether it is case 1 (dHa1) or 2 (dHa2). Some reactions have more than one step, as indicated by Col. (3) (Step No.). Energy units in kJ mol^{-1}.

Appendix F
W18 and W33 Transition State Energetics

Tables 8 and 9 shows transition-state properties for each reaction step and each radical–radical system, on top of the two ice models employed, W18 and W33.

Table 8
Data of the Transition States Found on the W18 Cluster Model at the BHLYP-D3(BJ)/6-31+G(d,p) Level

			ΔE_{TS}								
X/Y ··· W18	RX	TS #	ΔU	ΔD	$\Delta U + D$	ΔZPE	ΔH	$i\nu$ (cm^{-1})	ΔU (TZ)	ΔH (TZ)	T_c (K)
$CH_2OH + CH_2OH$	Rc		9.1	−4.8	4.3	0.3	**4.6**	−82.50	8.9	**4.4**	···
	dHa1		61.9	−7.7	54.2	−14.4	**39.8**	−1837.06	61.1	**39.1**	448.5
	dHa2	1	25.5	−0.8	24.7	−2.2	**22.5**	−60.69	23.6	**20.6**	···
	dHa2	2	26.8	−5.7	21.1	−11.4	**9.7**	−1461.84	44.4	**27.6**	394.3
$CH_3O + CH_3O$	Rc		16.2	−4.0	12.2	−0.5	**11.7**	−31.29	14.8	**10.3**	···
	dHa1		29.3	−3.6	25.7	−7.4	**18.3**	−863.13	26.9	**15.9**	212.9
	dHa2		33.6	−4.4	29.2	−8.2	**21.0**	−822.52	30.8	**18.2**	352.2
$CH_3 + CH_2OH$	Rc		2.8	−0.7	2.1	−0.1	**2.0**	−69.97	2.7	**1.9**	···
	dHa	1	28.2	−2.0	26.2	−0.6	**25.6**	−21.93	26.5	**23.9**	···
	dHa	2	47.0	−2.7	44.3	−11.7	**32.6**	−1226.28	46.6	**32.2**	295.7
$CH_3 + CH_3$	Rc		7.4	−5.4	2.1	−1.4	**0.7**	−36.520	6.6	**−0.1**	···
$CH_3 + CH_3O$	Rc		3.0	−1.5	1.5	−0.8	**0.7**	−88.820	2.5	**0.2**	···
	dHa		3.9	−1.9	2.0	−0.6	**1.3**	−129.30	3.5	**1.0**	36.1
$CH_3 + NH_2$	Rc		1.4	−1.0	0.4	−0.3	**0.0**	−19.83	1.2	**−0.1**	···
$HCO + CH_2OH$	Rc		6.8	−4.7	2.1	0.0	**2.2**	−55.33	6.3	**1.6**	···
	dHa1		5.0	−3.3	1.7	−1.6	**0.1**	−154.61	4.3	**−0.6**	26.2
	dHa2		46.9	−0.6	46.2	−13.7	**32.6**	−652.3997	45.0	**30.7**	153.7
$HCO + CH_3O$	Rc		8.9	−0.5	8.4	−2.1	**6.3**	−106.15	7.7	**5.1**	···
	dHa1		12.1	−5.3	6.8	−2.3	**4.5**	−228.50	10.8	**3.2**	57.8
	dHa2		23.0	−3.0	19.9	−6.6	**13.3**	−387.25	19.2	**9.6**	93.7
HCO + HCO	Rc		8.3	−2.7	5.6	−0.9	**4.7**	−75.94	7.6	**4.0**	···
	dHa1		6.3	−1.6	4.7	−1.4	**3.3**	−46.31	5.7	**2.7**	10.8
	dHa2		15.8	−0.9	14.9	−4.1	**10.8**	−102.29	13.3	**8.3**	8.3

Note. Pure DFT energies were refined at the BHLYP-D3(BJ)/6-311++G(2df,2pd) level (TZ). *U*, *D*, and ZPE stand for pure DFT, dispersion, and zero-point (vibrational) energies, respectively; *H* (in bold) is the combination of the three (i.e., enthalpies at 0 K); T_c is the tunneling crossover temperature. Col. (2) shows the reaction type, and for dHa whether it is case 1 (dHa1) or 2 (dHa2). Some reactions have more than one step, as indicated by Col. (3) (Step #). Energies in kJ mol^{-1}.

Table 9
Summary of All the Transition States Found in This Work at the BHLYP-D3(BJ)/6-31+G(d.p) Level

			ΔE_{TS}								
X/Y ···W33-cav	RX	TS #	ΔU	ΔD	$\Delta(U+D)$	ΔZPE	ΔH	$i\nu$ (cm^{-1})	ΔU (TZ)	ΔH (TZ)	T_c (K)
$CH_2OH + CH_2OH$	Rc	···	0.5	4.4	4.9	−1.8	**3.1**	28.78	0.0	**2.6**	···
	dHa1	1	0.8	2.0	2.8	−1.5	**1.3**	71.45	1.0	**1.4**	···
	dHa1	2	1.3	13.3	14.5	−3.9	**10.7**	−46.04	2.1	**11.6**	···
	dHa1	3	−1.4	14.4	13.0	−3.7	**9.2**	79.17	−1.6	**9.1**	···
	dHa1	4	10.7	18.5	29.2	−3.4	**25.7**	68.37	9.8	**24.9**	···
	dHa1	5	23.8	15.2	39.0	−10.9	**28.1**	542.54	24.7	**29.1**	154.7
	dHa2	1	10.6	−1.3	9.3	−0.4	**8.9**	95.87	10.6	**9.0**	···
	dHa2	2	26.6	−8.9	17.7	−11.0	**6.7**	1068.76	27.3	**7.4**	296.2
$CH_3O + CH_3O$	Rc	···	20.4	−2.3	18.1	2.8	**21.0**	140.15	19.5	**20.1**	···
	dHa1	···	22.1	−3.0	19.1	−5.9	**13.2**	886.62	20.6	**11.7**	225.7
	dHa2	···	32.2	−1.6	30.6	−4.9	**25.7**	788.36	27.8	**21.2**	189.8
$CH_3 + CH_2OH$	Rc	1	−1.6	4.5	3.0	−0.6	**2.4**	27.48	−1.4	**2.5**	···
	Rc	2	−2.8	1.6	−1.2	1.6	**0.4**	59.97	−2.7	**0.4**	···
	dHa	···	52.1	−0.4	51.7	−11.8	**39.9**	1020.12	51.2	**39.0**	242.0
$CH_3 + CH_3$	Rc	···	9.8	−2.5	7.2	−1.3	**5.9**	110.49	8.4	**4.6**	···
$CH_3 + CH_3O$	Rc	···	8.1	−3.8	4.3	0.1	**4.4**	123.81	6.8	**3.1**	···
	dHa	···	17.1	−2.9	14.2	−2.3	**11.9**	200.13	14.7	**9.5**	47.1
$CH_3 + NH_2$	Rc	···	1.4	−0.3	1.1	−0.4	**0.7**	92.25	1.1	**0.4**	···
$HCO + CH_2OH$	Rc	···	0.2	2.8	3.0	−1.3	**1.7**	55.18	0.2	**1.7**	···
	dHa1	···	1.9	1.2	3.2	−1.6	**1.6**	90.00	1.2	**0.8**	24.2
	dHa2	1	13.6	3.8	17.4	−2.2	**15.2**	35.32	10.6	**10.2**	···
	dHa2	2	37.4	0.5	37.9	−16.1	**21.7**	1321.28	36.0	**18.4**	387.0
$HCO + CH_3O$	Rc	···	2.4	2.3	4.7	−0.2	**4.5**	27.20	1.4	**3.5**	···
	dHa1	···	13.3	−4.8	8.6	−4.6	**4.0**	137.45	11.4	**2.0**	34.6
	dHa2	···	15.4	3.4	18.8	−3.6	**15.1**	188.68	13.4	**13.2**	35.4
HCO + HCO	Rc	···	6.7	−1.0	5.7	−0.7	**4.9**	64.27	5.8	**4.1**	···
	dHa1	1	9.0	−1.2	7.8	−1.5	**6.3**	119.03	6.7	**4.0**	28.4
	dHa2[a]	2	1.5	0.0	1.5	−1.7	**−0.3**	164.89	0.9	**−0.8**	29.6

Notes. See Section 4 for the full PESs. Pure DFT energies were refined at the BHLYP-D3(BJ)/6-311++G(2df,2pd) level (TZ). U, D, and ZPE stand for pure DFT, dispersion, and zero-point (vibrational) energies, respectively; H (in bold) is the combination of the three (i.e., enthalpies at 0 K); T_c is the tunneling crossover temperature. Col. (2) shows the reaction type, and for dHa whether it is case 1 (dHa1) or 2 (dHa2). Some reactions have more than one step, as indicated by Col. (3) (Step #). Energies in kJ mol^{-1}.

[a] The energy reference is point 24 from the backward intrinsic reaction coordinate calculation; see the figure sets in Figures 3 and 5, available online.

Appendix G
Spin Densities of Each Radical in Reactant Structures

Table 10 shows spin-density data for each of the reactant geometries studied in this work.

Table 10
Spin Densities of the Reactant Radical–Radical Structures

W18				
Reaction	R1	R2	SD R1	SD R2
Rc	CH3O	CH3O	−0.99655	1.00061
Rc	CH2OH	CH3	−0.99561	0.98991
Rc	CH3O	HCO	−1.00005	0.98816
Rc	CH2OH	CH2OH	−0.99358	0.99107
Rc	HCO	HCO	−0.99323	0.99112
Rc	CH3	CH3O	−0.99476	0.99810
Rc	HCO	CH2OH	−0.98802	0.99912
Rc	CH3	NH2	−0.99307	1.00575
dHa2	HCO	CH3O	−0.98813	1.00073
dHa	CH3	CH3O	−0.99352	0.99509
dHa2	HCO	CH2OH	−0.99078	0.99727
dHa2	CH3O	CH3O	−0.99985	0.99948
dHa2	CH3O	HCO	−0.99904	0.98953
dHa1	HCO	CH2OH	−0.98788	0.99898
dHa2	HCO	HCO	−0.98843	0.99094
dHa1	CH2OH	CH2OH	−0.99982	0.99592
dHa1	CH3O	CH3O	−1.00116	0.99809
dHa1	CH3O	HCO	−1.00104	0.98860
W33				
Reaction	R1	R2	SD R1	SD R2
Rc	CH3O	CH3O	−1.00019	1.00021
Rc	CH3O	HCO	−1.00020	0.99241
Rc	CH2OH	HCO	−0.98984	0.98981
Rc	CH2OH	CH2OH	−0.98789	0.99624
Rc	CH2OH	CH3	−0.99694	0.98891
Rc	CH2OH	CH3	−0.98978	0.98025
Rc	HCO	HCO	−0.97371	0.99443
Rc	CH3	CH3	−0.97903	0.98453
Rc	CH3	CH3O	−0.98658	0.99996
Rc	CH3	NH2	−0.98649	1.00420
dHa1	HCO	HCO	−0.97365	0.99442
dHa1	CH2OH	HCO	−0.98988	0.98980
dHa	CH3	CH3O	−0.98652	0.99999
dHa2	HCO	CH2OH	−0.98932	0.99573
dHa2	CH3O	CH3O	−0.99722	0.99942
dHa2	CH2OH	CH2OH	−0.99802	0.99996
dHa1	CH3O	HCO	−0.99924	0.97255
dHa1	CH3O	HCO	−0.99884	0.98571
dHa	CH2OH	CH3	−0.99693	0.98892
dHa1	CH2OH	CH2OH	−0.98764	0.99148
dHa1	CH3O	CH3O	−0.99668	0.99872
dHa2	HCO	CH3O	−0.98176	1.00135

Note. Computed employing natural bond population analysis. Figures of the spin densities and molecular orbitals are available online on Zenodo at doi:10.5281/zenodo.5723996.

Appendix H
S2 Values of Reactant and TS Structures

Tables 11 and 12 show values of the spin-squared operator for each of the studied reactant systems, before and after the automatic Gaussian spin annihilation step.

Table 11
$\langle S^2 \rangle$ Values before ($\langle S^2 \rangle_{bef}$) and after ($\langle S^2 \rangle_{aft}$) the Gaussian Spin Annihilation Step for the Reactant Structures of Each Studied Reaction on the W18 ASW Ice Model and on the Cavity of the W33 ASW Ice Model

W18				
Rad1	Rad2	Reaction	$\langle S^2 \rangle_{bef}$	$\langle S^2 \rangle_{aft}$
CH_3	CH_3	Rc	1.009	0.0720
CH_3	HCO	Rc/dHa	1.0101	0.0810
CH_3	NH_2	Rc	1.0089	0.0710
CH_3	CH_3O	Rc	1.0105	0.0841
CH_3	CH_3O	dHa	1.0093	0.0849
CH_3	CH_2OH	Rc	1.0086	0.0797
CH_3	CH_2OH	dHa	1.0086	0.0797
HCO	HCO	Rc/dHa1	1.0114	0.0913
HCO	HCO	dHa2	1.0113	0.0904
HCO	NH_2	Rc/dHa	1.0099	0.0797
HCO	CH_3O	Rc	1.0115	0.0920
HCO	CH_3O	dHa1	1.0113	0.0910
HCO	CH_3O	dHa2	1.0115	0.0919
HCO	CH_2OH	dHa2	1.0113	0.0910
HCO	CH_2OH	Rc	1.0113	0.0903
HCO	CH_2OH	dHa1	1.0113	0.0903
CH_3O	CH_3O	dHa1	1.0111	0.0937
CH_3O	CH_3O	dHa2	1.0118	0.0950
CH_3O	CH_3O	Rc	1.0112	0.0948
CH_2OH	CH_2OH	dHa1	1.0113	0.0906
CH_2OH	CH_2OH	Rc	1.0108	0.0894
CH_2OH	CH_2OH	dHa2	1.0114	0.0912
W33				
Rad1	Rad2	Reaction	$\langle S^2 \rangle_{bef}$	$\langle S^2 \rangle_{aft}$
CH_3	CH_3	Rc	1.0089	0.0723
CH_3	HCO	Rc/dHa	1.0102	0.0823
CH_3	NH_2	Rc	1.0082	0.0705
CH_3	CH_3O	Rc	1.0106	0.0847
CH_3	CH_3O	dHa	1.0106	0.0847
CH_3	CH_2OH	Rc	1.0100	0.0808
CH_3	CH_2OH	dHa	1.0100	0.0808
HCO	HCO	Rc	1.0114	0.0923
HCO	HCO	dHa1	1.0114	0.0923
HCO	NH_2	Rc/dHa	1.0095	0.0807
HCO	CH_3O	Rc	1.0116	0.0931
HCO	CH_3O	dHa1	1.0117	0.0937
HCO	CH_3O	dHa2	1.0116	0.0936
HCO	CH_2OH	Rc	1.0107	0.0880
HCO	CH_2OH	dHa1	1.0107	0.0880
HCO	CH_2OH	dHa2	1.0112	0.0923
CH_3O	CH_3O	Rc	1.0118	0.0951
CH_3O	CH_3O	dHa1	1.0096	0.0941
CH_3O	CH_3O	dHa2	1.0119	0.0955
CH_2OH	CH_2OH	Rc	1.0109	0.0871
CH_2OH	CH_2OH	dHa1	1.0021	0.0854
CH_2OH	CH_2OH	dHa2	1.0110	0.0887

Table 12

$\langle S^2 \rangle$ Values before ($\langle S^2 \rangle_{bef}$) and after ($\langle S^2 \rangle_{aft}$) the Gaussian Spin Annihilation Step for the Transition Structures of Each Studied Reaction on the W18 ASW Ice Model and on the Cavity of the W33 ASW Ice Model

W33				
Rad1	Rad2	Reaction	$\langle S^2 \rangle_{bef}$	$\langle S^2 \rangle_{aft}$
CH_3	CH_3	Rc	1.0072	0.0713
CH_3	HCO	Rc	1.0095	0.0813
CH_3	HCO	dHa	1.0104	0.0830
CH_3	NH_2	Rc	1.0088	0.0709
CH_3	CH_3O	Rc	1.0019	0.0807
CH_3	CH_3O	dHa	0.938	0.0820
CH_3	CH_2OH	Rc	0.996	0.0776
CH_3	CH_2OH	dHa (1)	1.0099	0.0793
CH_3	CH_2OH	dHa (2)	0.8359	0.0604
HCO	HCO	Rc	0.9927	0.0880
HCO	HCO	dHa1	1.0058	0.0921
HCO	HCO	dHa2	0.9993	0.0893
HCO	NH_2	Rc	0.9822	0.0733
HCO	NH_2	dHa	1.0054	0.0801
HCO	CH_3O	Rc	0.9949	0.0857
HCO	CH_3O	dHa1	0.9474	0.0766
HCO	CH_3O	dHa2	0.8249	0.0623
HCO	CH_2OH	Rc	0.9911	0.0848
HCO	CH_2OH	dHa1	1.0052	0.0885
HCO	CH_2OH	dHa2	0.9831	0.0831
CH_3O	CH_3O	Rc	0.9475	0.0717
CH_3O	CH_3O	dHa1	0.8639	0.0935
CH_3O	CH_3O	dHa2	0.8652	0.0942
CH_2OH	CH_2OH	Rc	0.9717	0.0774
CH_2OH	CH_2OH	dHa1	0.7698	0.0528
CH_2OH	CH_2OH	dHa2 (1)	1.0109	0.0882
CH_2OH	CH_2OH	dHa2 (2)	0.8024	0.0563

W33				
Rad1	Rad2	Reaction	$\langle S^2 \rangle_{bef}$	$\langle S^2 \rangle_{aft}$
CH_3	CH_3	Rc	0.9875	0.0675
CH_3	NH_2	Rc	0.9941	0.0677
CH_3	HCO	Rc	0.9866	0.0760
CH_3	HCO	dHa	0.9532	0.0726
CH_3	CH_3O	Rc	0.9872	0.0779
CH_3	CH_3O	dHa	0.9296	0.0822
CH_3	CH_2OH	Rc (1)	1.0101	0.0811
CH_3	CH_2OH	Rc (2)	0.9852	0.0739
CH_3	CH_2OH	dHa	0.8373	0.0582
HCO	HCO	Rc	0.9835	0.0864
HCO	HCO	dHa1	0.9753	0.0858
HCO	HCO	dHa2	1.0048	0.0912
HCO	CH_3O	Rc	1.0057	0.0898
HCO	CH_3O	dHa1 (1)	1.0117	0.0939
HCO	CH_3O	dHa1 (2)	0.9344	0.0772
HCO	CH_3O	dHa2	0.8876	0.0766
HCO	CH_2OH	Rc	1.011	0.0886
HCO	CH_2OH	dHa1	0.9695	0.0790
HCO	CH_2OH	dHa2 (1)	1.0111	0.0893
HCO	CH_2OH	dHa2 (2)	0.8068	0.0578
CH_3O	CH_3O	Rc	0.8303	0.0476
CH_3O	CH_3O	dHa1	0.8644	0.0940
CH_3O	CH_3O	dHa2	0.8697	0.0949
CH_2OH	CH_2OH	Rc	1.0109	0.0879
CH_2OH	CH_2OH	dHa1 (1)	1.0038	0.0856
CH_2OH	CH_2OH	dHa1 (2)	1.0113	0.0908
CH_2OH	CH_2OH	dHa1 (3)	1.0114	0.0919
CH_2OH	CH_2OH	dHa1 (4)	1.0084	0.0886
CH_2OH	CH_2OH	dHa1 (5)	0.7961	0.0473
CH_2OH	CH_2OH	dHa2 (1)	1.0093	0.0859
CH_2OH	CH_2OH	dHa2 (2)	0.7997	0.0530

Note. Values in parentheses for Col. (3) in Tables 11 and 12 correspond to the reaction step number if the channel is multistep.

Appendix I
Activation Energy and Temperature-dependent Efficiencies for Those Systems Not Explicitly Studied in This Work

Figures I1 and I2 present all the E_a- and T-dependent efficiencies for the systems: OH + CH_3/HCO/OH/NH_2/CH_3O/CH_2OH, NH + CH_3/HCO/OH/NH_2/CH_3O/CH_2OH, NH_2 + NH_2/CH_3O/CH_2OH, and CH_3O + CH_2OH. More details can be found in the main body of the article.

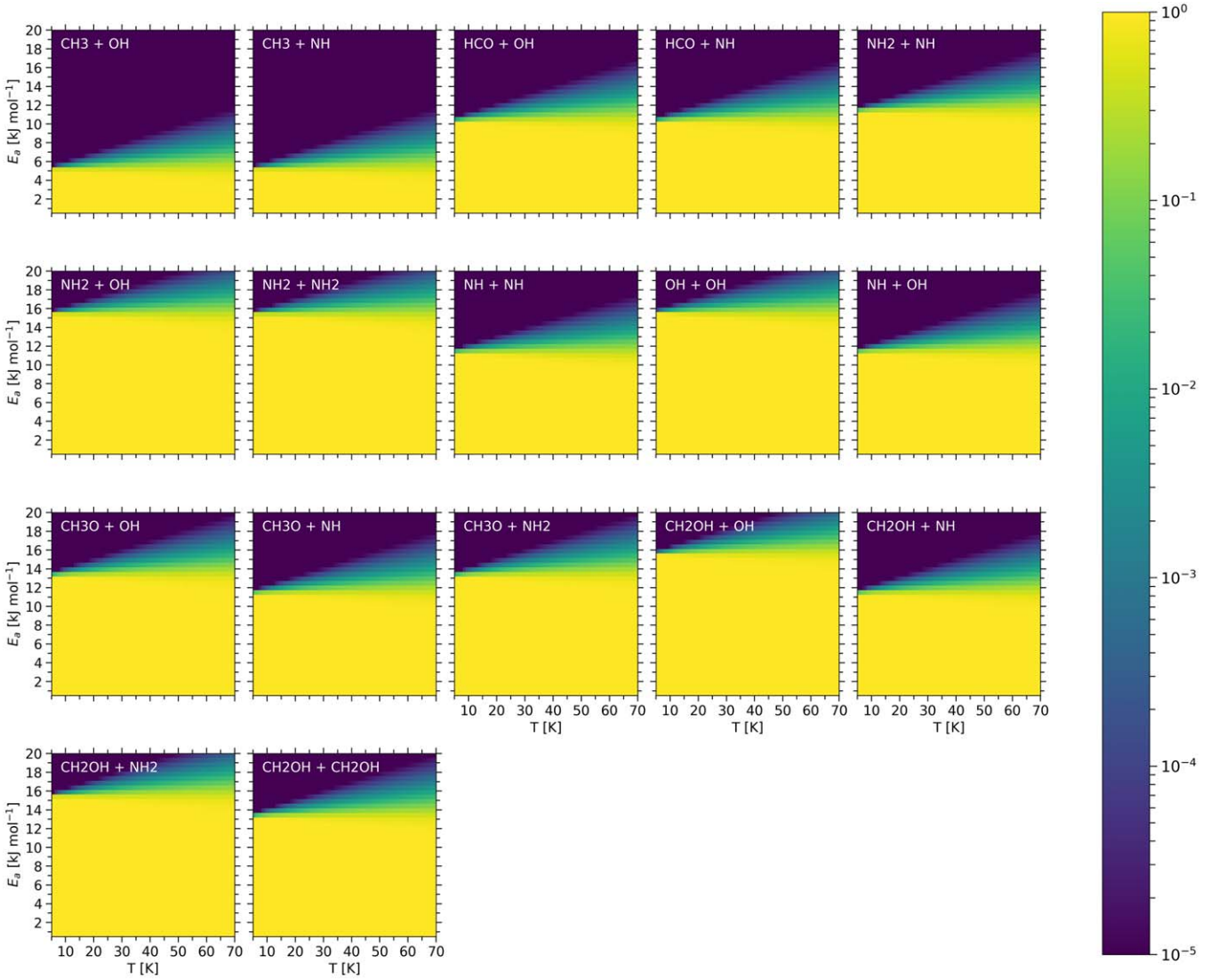

Figure I1. Reaction efficiencies on W33 as a function of activation energy and temperature of those radical–radical reactions in Garrod et al. (2008) not explicitly studied in this work.

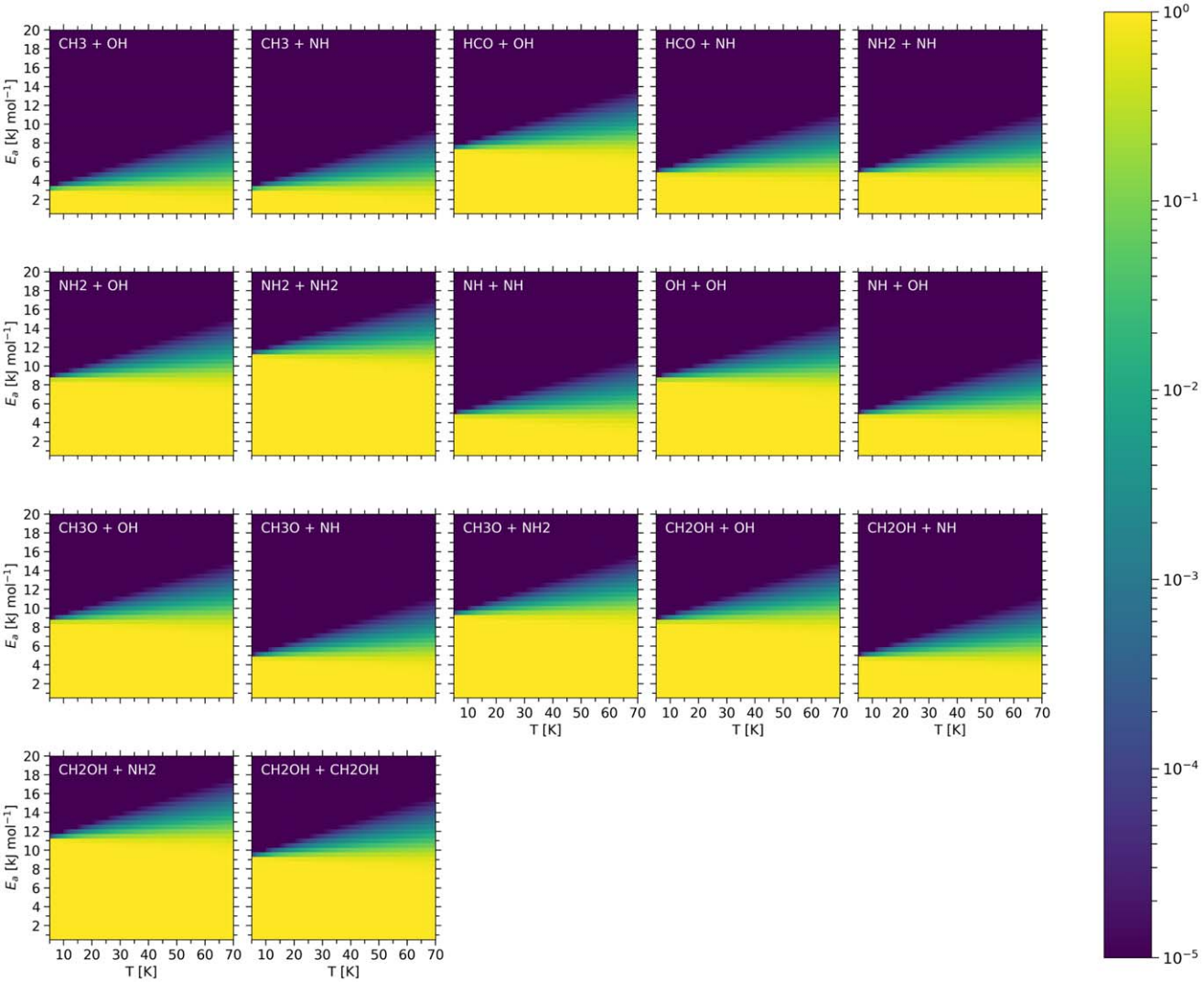

Figure I2. Reaction efficiencies on W18 as a function of activation energy and temperature of those radical–radical reactions in Garrod et al. (2008) not explicitly studied in this work.

Appendix J
Crossover Temperature Formula

In order to calculate the crossover temperatures (T_c), we have used Equation (J1) (Fermann & Auerbach 2000). At temperatures below T_c tunneling effects become dominant, and above it tunneling is negligible:

$$T_c = \frac{\hbar\omega^{\ddagger}\Delta H^{\ddagger}/k_{\rm B}}{2\pi\Delta H^{\ddagger} - \hbar\omega^{\ddagger}\ln(2)}, \quad \text{(J1)}$$

where $\hbar$ is the reduced Planck constant; $\omega^{\ddagger} = 2\pi\nu^{\ddagger}$, with $\nu^{\ddagger}$ the frequency (in absolute value) associated with the transition state; $\Delta H^{\dagger}$ is the ZPE-corrected energy barrier at 0 K; and $k_{\rm B}$ is the Boltzmann constant.

Appendix K
XYZ Structures

The XYZ data are available in a separate file uploaded to Zenodo at doi:10.5281/zenodo.5723996.

ORCID iDs

Joan Enrique-Romero https://orcid.org/0000-0002-2147-7735
Albert Rimola https://orcid.org/0000-0002-9637-4554
Cecilia Ceccarelli https://orcid.org/0000-0001-9664-6292
Piero Ugliengo https://orcid.org/0000-0001-8886-9832
Nadia Balucani https://orcid.org/0000-0001-5121-5683

References

Aikawa, Y., Furuya, K., Yamamoto, S., & Sakai, N. 2020, ApJ, 897, 110
Balucani, N., Ceccarelli, C., & Taquet, V. 2015, MNRAS, 449, L16
Becke, A. D. 1993, JChPh, 98, 1372
Bovolenta, G., Bovino, S., Vöhringer-Martinez, E., et al. 2020, MolAs, 21, 100095
Ceccarelli, C., Caselli, P., Fontani, F., et al. 2017, ApJ, 850, 176
Cernicharo, J., Marcelino, N., Roueff, E., et al. 2012, ApJL, 759, L43
Charnley, S. B., Tielens, A. G. G. M., & Rodgers, S. D. 1997, ApJL, 482, L203
Cheung, A. C., Rank, D. M., Townes, C. H., Thornton, D. D., & Welch, W. J. 1968, PhRvL, 21, 1701
Cheung, A. C., Rank, D. M., Townes, C. H., Thornton, D. D., & Welch, W. J. 1969, Natur, 221, 626
De Duve, C. 2005, Singularities: Landmarks on the Pathways of Life (Cambridge: Cambridge Univ. Press)
de Duve, C. 2011, RSPTA, 369, 620
Duflot, D., Toubin, C., & Monnerville, M. 2021, FrASS, 8, 24
Enrique-Romero, J., Álvarez-Barcia, S., Kolb, F. J., et al. 2020, MNRAS, 493, 2523
Enrique-Romero, J., Ceccarelli, C., Rimola, A., et al. 2021, A&A, 655, A9
Enrique-Romero, J., Rimola, A., Ceccarelli, C., et al. 2019, ESC, 3, 2158
Fermann, J. T., & Auerbach, S. 2000, JChPh, 112, 6787
Ferrero, S., Zamirri, L., Ceccarelli, C., et al. 2020, ApJ, 904, 11
Frisch, M. J., Trucks, G. W., Schlegel, H. B., et al. 2016, Gaussian16 Revision B.01 (Wallingford CT: Gaussian Inc.), https://gaussian.com/
Garrod, R. T., & Herbst, E. 2006, A&A, 457, 927
Garrod, R. T., & Pauly, T. 2011, ApJ, 735, 15
Garrod, R. T., Widicus Weaver, S. L., & Herbst, E. 2008, ApJ, 682, 283
Grimme, S., Antony, J., Ehrlich, S., & Krieg, H. 2010, JChPh, 132, 154104
Grimme, S., Ehrlich, S., & Goerigk, L. 2011, JCoCh, 32, 1456
Gutiérrez-Quintanilla, A., Layssac, Y., Butscher, T., et al. 2021, MNRAS, 506, 3734
Hariharan, P. C., & Pople, J. A. 1973, AcTC, 28, 213
Hasegawa, T. I., & Herbst, E. 1993, MNRAS, 263, 589
Hasegawa, T. I., Herbst, E., & Leung, C. M. 1992, ApJS, 82, 167
He, J., Emtiaz, S., & Vidali, G. 2018, ApJ, 863, 156
Hehre, W. J., Ditchfield, R., & Pople, J. A. 1972, JChPh, 56, 2257
Herbst, E., & van Dishoeck, E. F. 2009, ARA&A, 47, 427
Jensen, S. S., Jørgensen, J. K., Furuya, K., Haugbølle, T., & Aikawa, Y. 2021, A&A, 649, A66
Jin, M., & Garrod, R. T. 2020, ApJS, 249, 26
Kalvāns, J. 2018, MNRAS, 478, 2753
Karssemeijer, L. J., & Cuppen, H. M. 2014, A&A, 569, A107
Krishnan, R., Binkley, J. S., Seeger, R., & Pople, J. A. 1980, JChPh, 72, 650
Lamberts, T., Markmeyer, M. N., Kolb, F. J., & Kästner, J. 2019, ESC, 3, 958
Lee, C., Yang, W., & Parr, R. G. 1988, PhRvB, 37, 785
Martínez-Bachs, B., Ferrero, S., & Rimola, A. 2020, Int. Conf. on Computational Science and Its Applications (Berlin: Springer), 658
McQuarrie, D. 1976, Statistical Mechanics (New York: Harper and Row)
Minissale, M., Congiu, E., & Dulieu, F. 2016, A&A, 585, A146
Neese, F. 2004, JPCS, 65, 781
Penteado, E. M., Walsh, C., & Cuppen, H. M. 2017, ApJ, 844, 71
Rimola, A., Ceccarelli, C., Balucani, N., & Ugliengo, P. 2021, FrASS, 8, 38
Rimola, A., Skouteris, D., Balucani, N., et al. 2018, ESC, 2, 720
Rimola, A., Taquet, V., Ugliengo, P., Balucani, N., & Ceccarelli, C. 2014, A&A, 572, A70
Ruaud, M., Loison, J. C., Hickson, K. M., et al. 2015, MNRAS, 447, 4004
Ruaud, M., Wakelam, V., & Hersant, F. 2016, MNRAS, 459, 3756
Rubin, R. H., Swenson, G. W. J., Benson, R. C., Tigelaar, H. L., & Flygare, W. H. 1971, ApJL, 169, L39
Sameera, W. M. C., Senevirathne, B., Andersson, S., Maseras, F., & Nyman, G. 2017, J. Phys. Chem. C, 121, 15223
Senevirathne, B., Andersson, S., Dulieu, F., & Nyman, G. 2017, MolAs, 6, 59
Simons, M. A. J., Lamberts, T., & Cuppen, H. M. 2020, A&A, 634, A52
Skouteris, D., Balucani, N., Ceccarelli, C., et al. 2018, ApJ, 854, 135
Skouteris, D., Balucani, N., Ceccarelli, C., et al. 2019, MNRAS, 482, 3567
Snyder, L. E. 2006, PNAS, 103, 12243
Snyder, L. E., Buhl, D., Zuckerman, B., & Palmer, P. 1969, PhRvL, 22, 679
Taquet, V., Wirström, E. S., & Charnley, S. B. 2016, ApJ, 821, 46
Tielens, A. G. G. M., & Hagen, W. 1982, A&A, 114, 245
Vasyunin, A. I., Caselli, P., Dulieu, F., & Jiménez-Serra, I. 2017, ApJ, 842, 33
Vasyunin, A. I., & Herbst, E. 2013, ApJ, 769, 34
Vazart, F., Ceccarelli, C., Balucani, N., Bianchi, E., & Skouteris, D. 2020, MNRAS, 499, 5547
Viti, S., Collings, M. P., Dever, J. W., McCoustra, M. R. S., & Williams, D. A. 2004, MNRAS, 354, 1141
Wakelam, V., Loison, J. C., Mereau, R., & Ruaud, M. 2017, MolAs, 6, 22
Zamirri, L., Ugliengo, P., Ceccarelli, C., & Rimola, A. 2019, ESC, 3, 1499